Journal of
Materials Chemistry A

Materials for energy and sustainability

Accepted Manuscript

This article can be cited before page numbers have been issued, to do this please use: H. Parse, D. Sviri Belilty, B. Favelukis, M. Krämer, A. M. Mingers, S. Chakrabartty, N. Eliaz, B. Gault, D. Raabe, M. Sokol and B. A. Rosen, *J. Mater. Chem. A*, 2026, DOI: 10.1039/D6TA00700G.

ROYAL SOCIETY OF CHEMISTRY

rsc.li/materials-a

View Article Online
DOI: 10.1039/D6TA00700G

Extending the Electrochemical Stability Window of $Ti_3C_2T_z$ MXenes via Ta–Hf Co-Substitution for Durable Proton Exchange Membrane Fuel Cell Catalyst Supports

Haridas Parse[1,#], Danielle Sviri Belilty[1,#], Bar Favelukis[1], Mathias Krämer[2], Andrea M. Mingers[2], Sukanta Chakrabartty[1], Noam Eliaz[1], Baptiste Gault[2, 3], Dierk Raabe[2], Maxim Sokol[1] and Brian Rosen[1]*

1. Department of Material Science and Engineering, Tel Aviv University, Ramat Aviv, 69987001, Israel
2. Max Planck Institute for Sustainable Materials, Düsseldorf 40237, Germany
3. Present address: Univ Rouen Normandie, CNRS, INSA Rouen Normandie, Groupe de Physique des Matériaux, UMR 6634, F-76000 Rouen, France

# Equal contribution

* Corresponding Author: barosen@tauex.tau.ac.il

Abstract

MXenes are an emerging class of two-dimensional transition metal carbides with attractive electrical conductivity, surface chemistry tunability, and high surface area, making them promising candidates for electrocatalyst support materials in proton exchange membrane fuel cells. However, their practical use at positive electrochemical potentials is severely limited by rapid and irreversible oxidative degradation. Here, we demonstrate that introducing chemical disorder through oxyphilic metal co-substitution is an effective strategy to extend the electrochemical stability window of $Ti_3C_2T_z$ MXenes. Hafnium- and tantalum–hafnium co-substituted MAX phases were synthesized and converted to corresponding MXenes, enabling systematic investigation of single and co-substitution effects. X-ray photoelectron spectroscopy reveals that Ta-Hf co-substitution suppresses titanium oxide formation and stabilizes the surface chemistry of the MXene. Electrochemical corrosion measurements show that the corrosion potential of optimized Ta-Hf co-substituted MXenes shifts positively by up to 94 mV relative to pristine $Ti_3C_2T_z$, accompanied by reduced anodic currents and delayed passivation. Operando element-resolved dissolution measurements further confirm suppressed metal leaching under anodic polarization. When employed as catalyst supports in proton exchange membrane fuel cells, Pt-loaded Ta-Hf co-substituted MXenes exhibit significantly improved durability during accelerated stress testing. Specifically, the co-substituted MXene showed a 9 mV degradation, whereas the pristine MXene degraded by 39 mV. Additionally, Ta-Hf MXenes demonstrate superior stability under anode reversal conditions, outperforming

View Article Online
DOI: 10.1039/D6TA00700G

both unsubstituted and singly substituted MXenes. These results establish oxyphilic metal co-substitution as a general materials design strategy for stabilizing MXenes under anodic conditions, enabling their application as durable catalyst supports in advanced fuel cell systems.

Keywords: MAX, MXene, electrocatalyst, support material, PEM-fuel cell.

Introduction

The increase in global energy demand has drawn widespread attention to alternative technologies, including polymer electrolyte membrane fuel cells (PEMFCs).[1,2] Due to their high efficiency and low emissions, PEMFCs have garnered significant attention for their ability to directly convert green fuels, such as hydrogen, into electricity. Thereby reducing the dependence on fossil fuels.[3] Traditionally, platinum (Pt) and Pt-based alloys have been the most commonly used electrocatalysts for PEMFCs because they offer high exchange current density, chemical stability, and substantial work function.[3,4] In most cases, catalysts[2] used for PEMFCs are supported by conductive and nanoporous carbons.[5–7] Carbon-supported noble-metal-based catalysts demonstrate high activity and are considered the standard for advancements in fuel cell durability. However, carbon supports suffer from corrosion at potentials above 1.1 V vs RHE due to the parasitic oxidation of the carbon support to CO_2, which decreases the durability and lifetime of the fuel cell.[8–10] This degradation of the support is particularly evident during the frequent start-up and shut-down operations that mobile fuel cells endure, as opposed to stationary fuel cells.[11,12] Therefore, to improve the lifetime and durability of PEMFC fuel cells, the development of alternative support materials is highly desirable, as addressing catalyst-support degradation is essential for their practical implementation in PEMFCs.[13]

In the past decade, transition metal carbides (TMCs) have received significant attention as a class of electrocatalyst support material due to their high chemical stability in acidic environments, corrosion resistance, and excellent electrical conductivity. [1,14] MXenes, a class of 2D transition metal carbides, have gained significant interest in the electrocatalysis community in the field of energy storage and conversion.[15,16] MXene synthesis has often been carried out using selective engraving of the A-layer of the MAX phases $M_{n+1}AX_n$.[16–18] The general stoichiometric formula of MXene is written as $M_{n+1}X_nT_z$ where T_z represents

View Article Online
DOI: 10.1039/D6TA00700G

the surface functional groups such as -O, -OH or –F, etc.[19–22] To date, more than fifty distinct MXenes have been successfully prepared and reported.

Among MXenes, $Ti_3C_2T_z$ has gained the greatest attention owing to its relative ease of preparation, high surface area, high electrical and thermal conductivity, versatile intrinsic properties, hydrophilicity, and electrochemical activity.[23–28] $Ti_3C_2T_z$ undergoes oxidative degradation in a wide variety of environments, including atmospheric exposure[29,30], exposure to an oxidative gas[31] or liquid[32] or a positive electrochemical potential.[33] The mechanism of oxidation depends highly on the type of oxidative exposure and the physical state of the MXene.[34] The electrochemical oxidation of multilayer MXene flakes was studied in different electrolytes.[35,36] The corrosion behavior of single- and few-layer $Ti_3C_2T_z$ flakes were investigated in acidic electrolyte (1 M H_2SO_4), demonstrating that oxidation initiates at potentials above 0.3 V versus the saturated calomel electrode (SHE) and accelerates rapidly with increasing potential. It has been demonstrated that extensive anodic oxidation converts $Ti_3C_2T_z$ into electrochemically inactive TiO_2, causing severe loss of capacitance, whereas controlled low-potential partial oxidation preserves active Ti-C sites while creating enlarged interlayer spacing and nanoscale porosity. As a result, partial oxidation markedly enhances ion transport and high-rate electrochemical performance.[32,33]

The challenge is therefore to design MXene, which has an extended electrochemical window of stability over which its functionality is retained, and oxidation is controlled.[28] Among the strategies to achieve this goal is to substitute oxyphilic species at the M-site which can alter how the MXene flakes react under oxidative electrochemical conditions. Expanding the electrochemical window can therefore increase the number of applications for which MXenes can be used as electrocatalysts or electrocatalyst supports.

To control the electrochemical oxidation of $Ti_3C_2T_z$, single and multi-transition-metal substitutions were introduced into $Ti_3C_2T_z$ MXenes derived from triple transition metal-substituted 312 MAX phases.[30–32] Moreover, single transition metal atom substitution improve the electrochemical oxidation performance but usually provide only limited resistance to electrochemical oxidation.[37] The multiple transition metal-substituted MAX phases are the most widespread solid solutions.[38,39] Altering the MAX phases and MXenes

View Article Online
DOI: 10.1039/D6TA00700G

by substituting different transition metal atoms can improve or customize their optical, electronic, thermal, mechanical, and electrochemical properties.[40-43]

Herein, we have studied the electrochemical oxidation of $Ti_3C_2T_z$ before and after 5 at% and 10 at% hafnium (Hf) and tantalum-hafnium (Ta-Hf) co-substitution (for example, $Ti_{2.85}Ta_{0.075}Hf_{0.075}C_2T_z$ and $Ti_{2.7}Ta_{0.15}Hf_{0.15}C_2T_z$) in 0.5 M H_2SO_4 at oxidizing potentials above the reversible hydrogen electrode (RHE). Ta and Hf elements can form strong metal-carbon and metal-oxygen bonds within the MXene skeleton, thereby improving the material's stability and preventing oxidative degradation in corrosive environments.[44] Moreover, Ta and Hf are very well known for the formation of a stable protective oxide layer.[45] Furthermore, the influence of the Ta and Hf co-doping in the MXene significantly improved the durability of the PEMFCs catalyst support. Therefore, multi-substituted MXenes increases the chemical variety of MXenes which can be studied, and therefore work such as ours which show synergy between multiple substitutions can encourage many more future studies using other variations.

Experimental Section

Materials

Titanium (Ti, 99.8%), aluminum (Al, 99.7%), and lithium fluoride (LiF, 99.7%), powders were acquired from Strem Chemicals and utilized as is. Tantalum (Ta), titanium carbide (TiC), and hafnium (Hf) were procured from Alfa Aesar. Hexachloroplatinic acid ($H_2PtCl_6 \cdot 6H_2O$, >37.5% Pt) was obtained from Merck. Hydrochloric acid (HCl, 32%), sulfuric acid (H_2SO_4, 95-98%), isopropanol (IPA), and ethylene glycol (EG), were sourced from Lab-Chem. SIGRACET GDL 28BC carbon paper gas diffusion layer (GDL) and a single-sided Pt/C-coated Nafion NR-212 membrane, and a 20% Nafion solution, were purchased from Ion-Power (USA). Deionized (DI) water generated by a Milli-Q system was used in all experiments and the electrochemical study.

Ti_3AlC_2, $Ti_{3-x}Hf_xAlC_2$ and $Ti_{3-2x}Ta_xHf_xAlC_2$ MAX phase synthesis

Ti_3AlC_2 synthesis

TiC, Ti, Ta, Hf and Al powders were used to synthesize MAX phases with Hf and Ta-Hf co-substitution such as Ti_3AlC_2, $Ti_{3-2x}Hf_xAlC_2$, and $Ti_{3-2x}Ta_xHf_xAlC_2$. Initially, Ti_3AlC_2 was synthesized using a molar ratio of 2:1:1.15 for TiC:Ti:Al. The powders were mixed

View Article Online
DOI: 10.1039/D6TA00700G

using ball milling (5 min at 1800 rpm) to obtain a homogeneous mixture. 5 g of the resulting mixture was cold-pressed into 20 mm diameter pellets under a uniaxial pressure of 50 MPa. The resulting pellet was placed in an alumina boat with an alumina lid and transferred to the tubular furnace for high-temperature synthesis. The pellet was annealed at 1500 °C (heating rate: 5 °C/min) for 2 h in a protective atmosphere using argon (Ar) with a 200 sccm flow rate and a small amount of Ti powder, which served as a sacrificial oxidizing agent to prevent undesired oxidation of the MAX phase. The pellet was then crushed and ball-milled at 1800 rpm to obtain a powder with a uniform particle size of 25 µm. Finally, the resulting powder was stirred overnight in HCl (9M) and washed with DI water several times to avoid the impurities, and the final product was verified as Ti_3AlC_2.

$Ti_{3-x}Hf_xAlC_2$ and $Ti_{3-2x}Ta_xHf_xAlC_2$ synthesis

Synthesis of the phases substituted with Hf and Hf-Ta were prepared using a similar procedure as outlined above. To obtain targeted solid MAX phases of $Ti_{2.85}Hf_{0.15}AlC_2$, $Ti_{2.7}Hf_{0.3}AlC_2$, $Ti_{2.85}Ta_{0.075}Hf_{0.075}AlC_2$ and $Ti_{2.7}Ta_{0.15}Hf_{0.15}AlC_2$ (312 MAX phases), powders of TiC, Ti, Ta, Hf, and Al were mixed in the molar ratios given in Table 1.

Table 1: Precursor molar ratios for targeted MAX phase synthesis.

Sample Name	Molar ratio of the elements				
	Ti	Al	TiC	Ta	Hf
Ti_3AlC_2	1	1.15	2	-	-
$Ti_{2.85}Hf_{0.15}AlC_2$	0.85	1.15	2	-	0.15
$Ti_{2.7}Hf_{0.3}AlC_2$	0.7	1.15	2	-	0.3
$Ti_{2.85}Ta_{0.075}Hf_{0.075}AlC_2$	0.85	1.15	2	0.075	0.075
$Ti_{2.7}Ta_{0.15}Hf_{0.15}AlC_2$	0.7	1.15	2	0.15	0.15

MXene synthesis

The synthesis of MXenes $Ti_3C_2T_z$, $Ti_{2.85}Hf_{0.15}C_2T_z$, $Ti_{2.7}Hf_{0.3}C_2T_z$, $Ti_{2.85}Ta_{0.075}Hf_{0.075}C_2T_z$ and $Ti_{2.7}Ta_{0.15}Hf_{0.15}C_2T_z$, were carried out using selective etching of the Al layer from the as-synthesized Ti_3AlC_2, $Ti_{2.85}Hf_{0.15}AlC_2$, $Ti_{2.7}Hf_{0.3}AlC_2$, $Ti_{2.85}Ta_{0.075}Hf_{0.075}AlC_2$, and $Ti_{2.7}Ta_{0.15}Hf_{0.15}AlC_2$ parent MAX phases. Typically, 500 mg of the Ti_3AlC_2 MAX phase

View Article Online
DOI: 10.1039/D6TA00700G

was added to a solution comprising 800 mg of LiF and 10 mL of concentrated HCl and stirred at 45 °C in an oil bath for 24 h. Similarly, Hf-substituted MXene were synthesized. For Ta-Hf co-substituted Max phases, 500 mg of Ta-Hf co-substituted MAX phase powder was mixed to the solution containing 2000 mg of LiF and 30 mL of concentrated HCl and vigorously stirred at 45 °C for 24 h. Etching conditions for pristine Ti_3AlC_2 differ from the Ta-Hf co-substituted MAX phases due to the changes in the bonding environment. Co-substitution of Ti with Ta and Hf alters the M-A bonding. This co-substitution increases the overall stability of the MAX phases and reinforce the interaction between Al layer and transition metal layer. Therefore, the co-substituted MAX requires a higher concentration *in-situ* generated HF to successfully remove the Al layer to yield corresponding MXenes.[46] After the etching process, the resulting mixture was washed with deionized (DI) water and spun down in a centrifuge at 7500 rpm for 5 minutes per cycle until the pH of the supernatant reached 7. The supernatant was collected, sonicated in an ice-cold bath sonicator for 30 min, followed by another round of centrifugation at 7500 rpm for 30 min. The resulting supernatant contained single flakes of $Ti_3C_2T_z$, $Ti_{2.85}Hf_{0.15}C_2T_z$, $Ti_{2.7}Hf_{0.3}C_2T_z$, $Ti_{2.85}Ta_{0.075}Hf_{0.075}C_2T_z$ or $Ti_{2.7}Ta_{0.15}Hf_{0.15}C_2T_z$. Vacuum filtration (Celgard 3105) was used on the supernatant to prepare free-standing films.

Synthesis of $Pt/Ti_3C_2T_z$, $Pt/Ti_{2.85}Hf_{0.15}C_2T_z$, $Pt/Ti_{2.7}Hf_{0.3}C_2T_z$, $Pt/Ti_{2.85}Ta_{0.075}Hf_{0.075}C_2T_z$ and $Pt/Ti_{2.7}Ta_{0.15}Hf_{0.15}C_2T_z$

Platinum (Pt) was loaded onto the surface of the MXenes at a mass of 40 wt% using the polyol method. Specifically, 45 mg of MXenes such as $Ti_3C_2T_z$, $Ti_{2.85}Hf_{0.15}C_2T_z$, $Ti_{2.7}Hf_{0.3}C_2T_z$, $Ti_{2.85}Ta_{0.075}Hf_{0.075}C_2T_z$ and $Ti_{2.7}Ta_{0.15}Hf_{0.15}C_2T_z$ was taken in a 50 ml centrifuge tube, followed by 2 mL of $H_2PtCl_6 \cdot 6H_2O$ (30 mg/mL) solution was added. The mixtures were sonicated for 15 min.

View Article Online
DOI: 10.1039/D6TA00700G

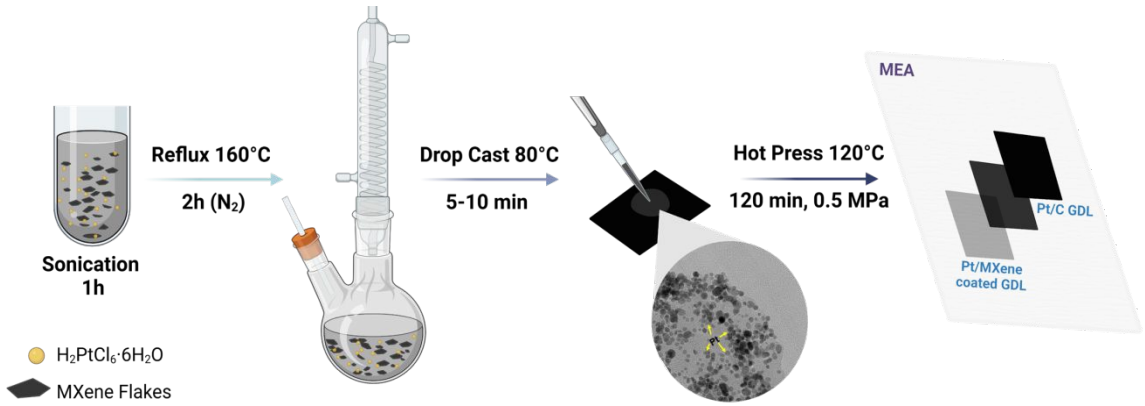

Scheme 1. Schematic representation of the synthesis of the Pt/MXene using polyol method. Created with BioRender.com.

Afterwards, 50 mL of EG was added to the above mixture and purged with N_2 gas for 15 minutes, after which the mixture was placed in a bath sonicator for 1 h. The resulting solution was transferred to a three-necked round-bottom flask and refluxed at 160 °C for 2 h under a protective nitrogen atmosphere, with vigorous stirring in an oil bath. After cooling to room temperature, the obtained powders were washed several times with an ethanol-water mixture (40:10 v/v) using a centrifuge at 7000 rpm for 5 min for each cycle and finally washed with pure ethanol. The obtained Pt/MXene powders were dried overnight at 80 °C and used for further studies.

Structural and Chemical Characterization

The PANalytical diffractometer (Aeris research edition) with a Cu Kα X-ray radiation source (λ = 1.5406 Å) in the range of 5-70° 2θ with a step size of ~0.01087° 2θ and scan speed ~0.0557° 2θ /sec was used to obtain the XRD patterns. The JEOL (IT200) and Quanta 200FEGESEM scanning electron microscope (SEM) with an energy-dispersive spectroscopy (EDS) detector was used to investigate the microstructure and the elemental analysis of the prepared samples. Atomic-scale characterization of the MAX lamellae FIB samples was carried out by high-resolution scanning transmission electron microscopy (HR-STEM), using a Cs-corrected (S-CORR) probe operating at 200 kV (Thermo Fisher Scientific Spectra 200). TEM and STEM modes using a high-angle annular dark field (HAADF) detector were used to record the material images. The EDS spectra were collected with a Super-X (Thermo Fisher Scientific) silicon drift detector (SDD). The images and the EDS spectra were processed with Thermo Fisher Scientific Velox software (version 3.14).

View Article Online
DOI: 10.1039/D6TA00700G

X-ray photoelectron spectroscopy (XPS) measurements were carried out under ultra-high vacuum (UHV) conditions with a base pressure of 2.5×10^{-10} Torr, using a 5600 Multi-Technique System (PHI, USA). The samples were irradiated with an Al Kα monochromatic source (1486.6 eV), and the emitted electrons were analyzed with a Spherical Capacitor Analyzer equipped with a 0.8 mm slit aperture. The binding energy scale was calibrated to C1s peak at 284.8 eV. Spectra were fitted using mixed Gaussian–Lorentzian line shapes after Shirley background subtraction. Peak deconvolution was performed using constraints on peak positions, area ratios, and spin-orbit splitting based on literature values.

Operando Element-Resolved Dissolution Measurements

Operando electrochemical experiments were performed using a scanning flow cell (SFC) connected to a potentiostat (Reference 600, Gamry Instruments) and an inductively coupled plasma-mass spectrometer (ICP-MS, NexION 300X, Perkin Elmer) for time- and potential-resolved analysis of dissolved ion concentrations (47Ti, 178Hf, 181Ta). The SFC, consisting of 400 µm V-shaped channels with the electrolyte outlet connected to the ICP-MS, was pressed with 200 mN onto the free-standing MXene films used as the working electrode, exposing a geometric area of approximately 0.178 mm². A Pt tube (0.38 mm diameter) was used as the auxiliary electrode and placed in the inlet channel, while a silver-silver chloride (Ag/AgCl) electrode in 3 M KCl positioned in the outlet channel served as the reference electrode. A 0.1 M H_2SO_4 electrolyte was prepared from H_2SO_4 (96%, Merck) and deionized water (PureLab Flex2, Elga, 18MΩ cm-1, TOC < 3ppb), and pumped with a flow rate of approximately 170 µL min^{-1} through the cell. Due to the high dissolution of Hf and Ta, these elements were electronically diluted using the band pass mass filter of the Dynamic Reaction Cell of the ICP-MS. The electrochemical protocol started with a 600 s open-circuit potential (OCP) hold, after the sample was brought into contact with the electrolyte. The potential was then ramped to 1.2 V vs RHE at a scan rate of 1 mV s^{-1}.

Electrochemical Measurements

The Biologic VSP-300 potentiostat was used to examine the electrochemical performance of the synthesized MXenes. Electrochemical corrosion studies were carried out using a typical three-electrode system with 0.5 M H_2SO_4 as the electrolyte. As-prepared materials

View Article Online
DOI: 10.1039/D6TA00700G

coated on a glassy carbon (GC) rotating disk electrode (RDE, area=0.19625 cm^2) were used as the working electrode. The working electrode was prepared using the drop-casting method. A freshly prepared 20 µl MXene colloidal solution (0.2 g/l) was drop-cast onto a cleaned GC disk coated with diamond slurry and subsequently dried at room temperature. An Ag/AgCl saturated KCl electrode and a Pt wire were employed as the reference and auxiliary electrodes, respectively. The potentiodynamic oxidation studies of all the MXenes were carried out by varying the potential from 0.2 to 1.2 V vs RHE at a potential sweep rate of 0.167 mV/s. Open-circuit potential (OCP) tests were performed for 3 h prior to each measurement to ensure system equilibrium.

The electrochemical oxidation of MXenes carried out using three electrode system. Where, as synthesized MXene flakes drop casted on the gold coated TEM grid and wrapped in the Pt mesh and used as working electrode. The electrochemical oxidation carried out at the potential range of 0 to 0.9 V vs RHE with the scan rate of 0.167 mV/s in 0.5 M H_2SO_4. The Pt wire and Ag/AgCl used as counter and reference electrode. Further, TEM images were acquired before and after electrochemical oxidation to evaluate the morphological changes and degradation pattern.

An electrochemical quartz crystal microbalance (EQCM) with a QSD-300 (Biologic) was used to investigate mass changes during electrochemical oxidation. A 4 µg MXene-loaded quartz crystal coated with Au/Ti (10 MHz frequency and sensitivity of 0.0815 ng/Hz·cm^2) was used as the working electrode. A platinum wire and Ag/AgCl, saturated KCl electrode served as the auxiliary and reference electrode, respectively. All the experiments were carried out in 0.5 M H_2SO_4 electrolyte solution.

Membrane electrode assembly (MEA)

The gas diffusion electrodes (GDEs) were fabricated using 5 cm^2 square-shaped carbon paper. As obtained catalysts Pt/$Ti_3C_2T_z$, Pt/$Ti_{2.85}Hf_{0.15}C_2T_z$, Pt/$Ti_{2.85}Hf_{0.30}C_2T_z$, Pt/$Ti_{2.85}Ta_{0.075}Hf_{0.075}C_2T_z$, and Pt/$Ti_{2.7}Ta_{0.15}Hf_{0.15}C_2T_z$ were used to fabricate the anodes for PEM-FC. Typically, 4 mg of each catalyst was dispersed in 1 ml of a solution comprising IPA, water, and Nafion in a 1:1:0.01 volume ratio. To obtain homogenous dispersion, the mixture was sonicated for 30 min in an ice-cold bath sonicator. The microporous layers of carbon paper were drop-casted with the resulting catalyst dispersion and dried on a hot plate at 80 ^oC. A commercially available Pt/C catalyst coated Nafion

View Article Online
DOI: 10.1039/D6TA00700G

NR-212 membrane (0.3 mg Pt/cm^2) was employed as the cathode, while blank carbon paper (5 cm^2) was used on the back side of the Pt/C coated catalyst as a support. The Pt loading of all GDEs was maintained at 0.3 mg/cm^2. Further, hot-pressing was used to fabricate the membrane electrode assembly (MEA) by pressing the GDEs and the NR-212 membrane at 120 °C for 120 seconds under 1 MPa.

The 850e fuel cell test workstation (Scribner Associates Inc., North Carolina, USA) was used to evaluate the fuel cell performance. A full cell assembly consists of a 5 cm^2 working area of the commercial single-fuel cell, with PTFE gaskets of 230 μm thickness at the cathode and anode. Measurements of the fuel cell were recorded at a working temperature of 80 °C, with oxygen (O_2, 0.2 L/min) provided as oxidant to the cathode and humidified hydrogen (H_2, 0.2 L/min) supplied to the anode as fuel. Subsequently, the cell was conditioned using a break-in process before each measurement. The break-in process involved cycling the cell potential consecutively between 0.6 V (2 min.) and 0.35 V (2 min).

PEM Fuel Cell Testing

Finally, accelerated stress tests (AST) and anode reversal tests were performed with a Biologic VSP-300 to evaluate the stability of catalysts such as Pt/$Ti_3C_2T_z$, Pt/$Ti_{2.85}Ta_{0.075}Hf_{0.075}C_2T_z$, and Pt/$Ti_{2.7}Ta_{0.15}Hf_{0.15}C_2T_z$. The ASTs were performed at an operating temperature of 80 ^oC with a supply of fully humidified H_2 and N_2 to the anode and cathode, respectively. The stability test consisted of 20,000 (20k) cycles using chronoamperometric technique, cycling between a holding potential of 0.6 V (3 seconds) and 0.9 V (3 seconds). The stability of each catalyst was assessed by comparing polarization curves recorded before and after the 20k cycles.

Results and Discussion

Structural Characterization of MAX Phases

XRD analysis was carried out to determine the crystallographic properties and phase of the $Ti_{3-x}Hf_xAlC_2$- and $Ti_{3-2x}Ta_xHf_xAlC_2$-type MAX phases with different Hf, Ta compositions (for Hf doping x = 0.15, 0.3 and for Ta, Hf co-doping x = 0.075 and 0.15). **Figure 1** shows the comparative X-ray powder diffractograms of Ti_3AlC_2, $Ti_{2.85}Ta_{0.075}Hf_{0.075}AlC_2$, $Ti_{2.7}Ta_{0.15}Hf_{0.15}AlC_2$, $Ti_{2.85}Hf_{0.15}AlC_2$ and $Ti_{2.7}Hf_{0.3}AlC_2$. As-synthesized pristine Ti_3AlC_2

View Article Online
DOI: 10.1039/D6TA00700G

shows good agreement with previously reported XRD pattern in literature.[47,48] **Figure 1(b)** reveals a clear shift in peaks (as represented by the dominant (104) reflection) towards lower 2θ angles due to lattice expansion upon substitution of Ti with larger atom Hf and Ta (5d element) with larger electronic cloud.[37] XRD also confirms that the substituted MAX phases retained the same structure as the pristine material, with only a small amount of secondary TiC phase (PDF-01-089-3828) indicated by an asterisk in **Figure 1(a)**. **Figure S1** shows the XRD patterns of synthesized free-standing $Ti_3C_2T_z$, $Ti_{2.85}Hf_{0.15}C_2T_z$, $Ti_{2.7}Hf_{0.3}C_2T_z$ $Ti_{2.85}Ta_{0.075}Hf_{0.075}C_2T_z$, and $Ti_{2.7}Ta_{0.15}Hf_{0.15}C_2T_z$ MXene films, which confirm the basal plane alignment and 2D carbide crystal structure.[49,50] Moreover, it confirms the absence of the other crystalline phases (**Figure S1**). Unlike MAX phases, the shift of the (002) peak for $Ti_{2.7}Ta_{0.15}Hf_{0.15}C_2T_z$ and $Ti_{2.85}Ta_{0.075}Hf_{0.075}C_2T_z$ samples is mainly attributed to variations in the interlayer water content, consistent with the hydration-sensitive (002) reflection of $Ti_3C_2T_z$ MXene rather than a fundamental change in the MXene crystal lattice.[51]

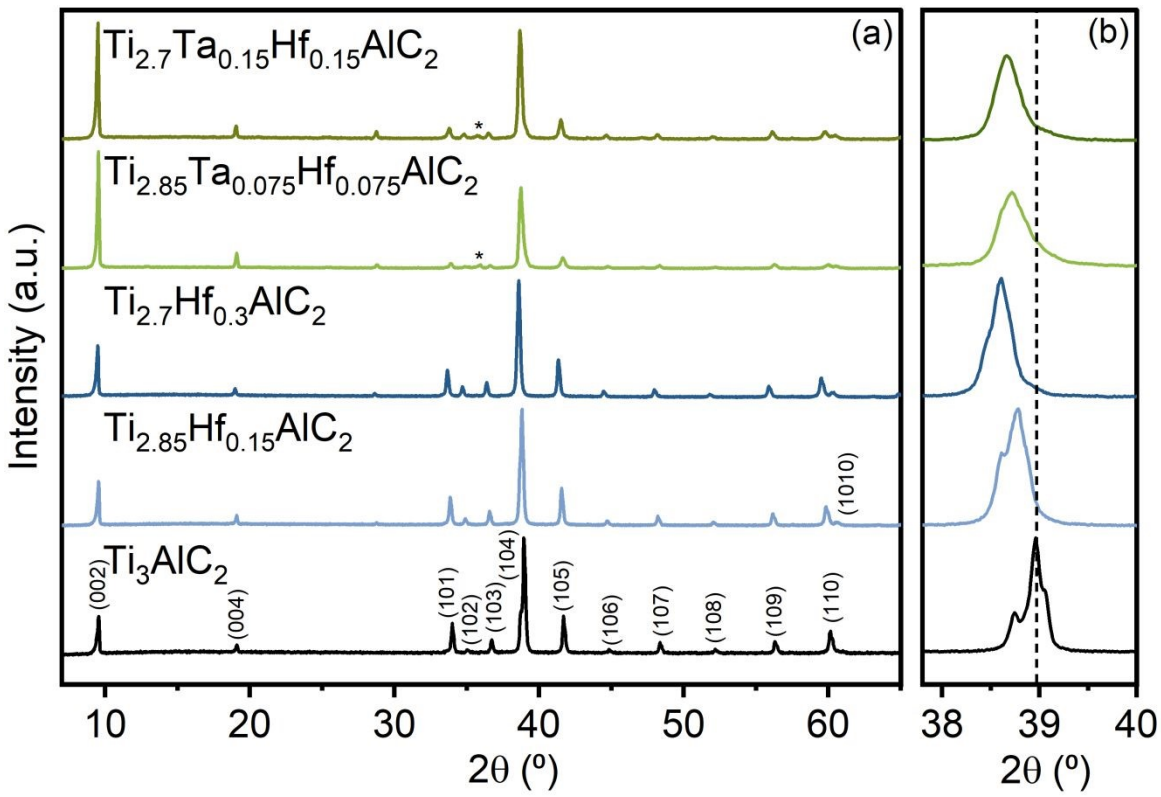

View Article Online
DOI: 10.1039/D6TA00700G

Figure 1. *XRD analysis. (a) Comparative XRD patterns of as-prepared powders targeted to MAX phase ($Ti_{3-x}Hf_xAlC_2$), ($Ti_{3-2x}Ta_xHf_x$)3AlC2 with change in Ta and Hf content (x=0, 0.075, 0.15, and 0.3). (* indicate TiC; secondary phase) (b) Zoomed in portion of high intensity peak at 2Θ value of 30-41°, which depict the expansion of the lattice parameter.*

Morphology and Atomic Structure Characterization of MAX Phases

The SEM, high-resolution scanning electron microscopy (HR-SEM), TEM, and STEM were all used to investigate the morphology and atomic structure of $Ti_{2.85}Ta_{0.075}Hf_{0.075}AlC_2$, $Ti_{2.7}Ta_{0.15}Hf_{0.15}AlC_2$, $Ti_{2.85}Hf_{0.15}AlC_2$ and $Ti_{2.7}Hf_{0.3}AlC_2$. **Figure S2** shows SEM images of the Hf-substituted MAX phases, where a representative layered structure was observed resembling pristine Ti_3AlC_2. The lateral distribution of Ta and Hf in the as-prepared Ta-Hf co-substituted MAX phases was confirmed using SEM-EDS as well as TEM-EDS analysis, as revealed in **Figures S3-S5.**

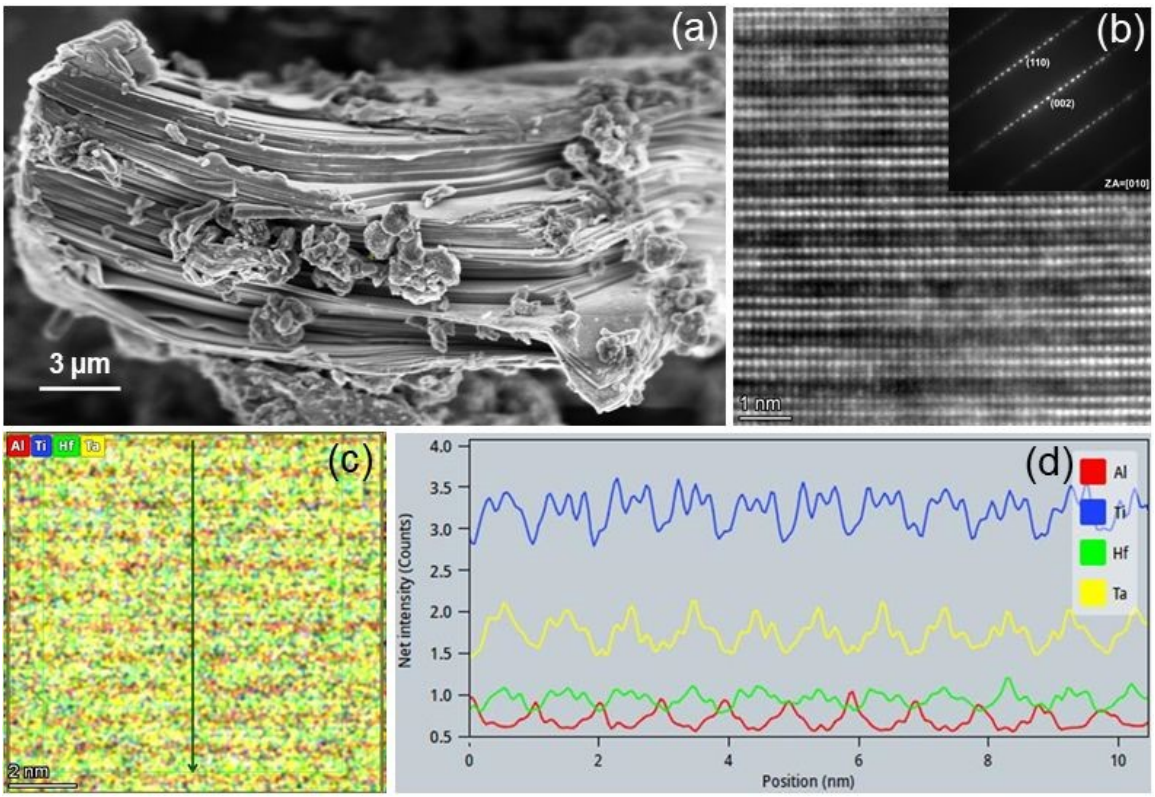

Figure 2. *Morphological and atomic scale characterization of $Ti_{2.7}Ta_{0.15}Hf_{0.15}AlC_2$ solid solution MAX phase. (a) The HR-SEM image of the $Ti_{2.7}Ta_{0.15}Hf_{0.15}AlC_2$ particle (b) atomic structure viewed along zone axis [010] of $Ti_{2.7}Ta_{0.15}Hf_{0.15}AlC_2$ using high resolution STEM, (c-d) EDS compositional line profiles obtained from elemental mapping.*

View Article Online
DOI: 10.1039/D6TA00700G

The co-substituted $Ti_{2.7}Ta_{0.15}Hf_{0.15}AlC_2$ MAX phase was studied using various microscopic techniques to learn about the atomic structure and cross-sectional distribution of the substituting atoms. A typical layered MAX phase morphology of $Ti_{2.7}Ta_{0.15}Hf_{0.15}AlC_2$ was confirmed by HR-SEM in **Figure 2(a)**.[52] Moreover, clear visuals of the atomic layers of $Ti_{2.7}Ta_{0.15}Hf_{0.15}AlC_2$, observed from the [010] zone axis, were provided by STEM and are shown in **Figure 2(b)**. The Z-contrast between the inner and outer layers of the substituted carbides was observed using HAADF imaging, as depicted in **Figure 2(b)**. Further, the inset of Figure 2(b) shows the selected-area electron diffraction (SAED) pattern, corroborating the crystallographic planes identified by XRD in **Figure 1(a)**.

Interestingly, the line profile in **Figure 2(c-d)** shows that Ti and Hf were present in approximately equal amounts among the metal layers of the MAX phase (i.e., had no preferential partitioning), whereas Ta was strongly concentrated within the middle metal layer. Previous studies by the co-authors have reported selective Ta distribution in the middle layer; however, here it is shown that this effect is unchanged even with the addition of Hf to the MXene (which did not show the segregation effect).[53] Such a differentiation may lead to differential chemical properties of the co-substituted MXenes as the relative amounts of Hf and Ta are changed.[34]

Structural and Chemical Characterization of MXenes

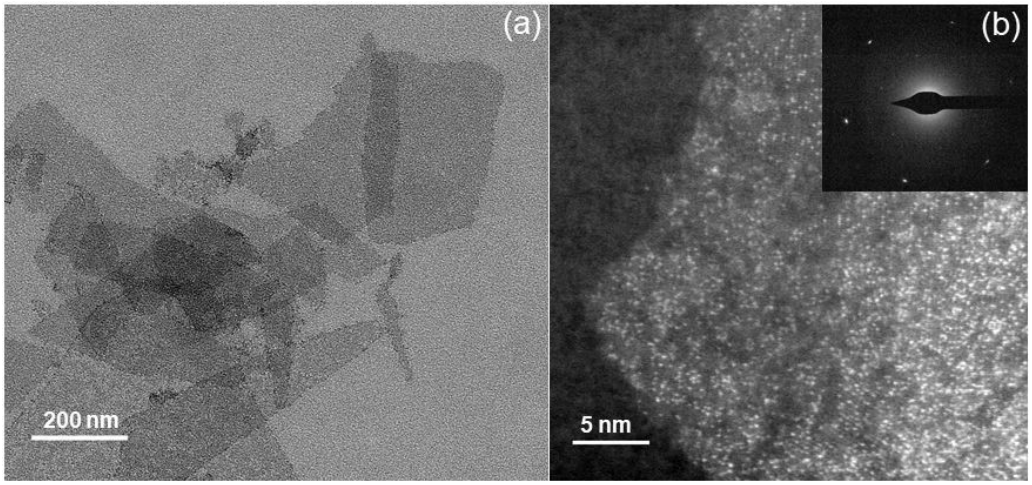

View Article Online
DOI: 10.1039/D6TA00700G

Figure 3. *Morphological and atomic scale characterization of the solid solution $Ti_{2.7}Ta_{0.15}Hf_{0.15}C_2T_z$ MXene. (a) TEM image the $Ti_{2.7}Ta_{0.15}Hf_{0.15}C_2T_z$ (b) The STEM image of single flake of MXene and corresponding SAED patterns in inset.*

Furthermore, TEM and STEM were used to analyze the atomic structure of the $Ti_{2.7}Ta_{0.15}Hf_{0.15}C_2T_z$, the MXene with the largest level of substitution among the materials studied. **Figure 3(a)** reveals the single few flakes of the $Ti_{2.7}Ta_{0.15}Hf_{0.15}C_2T_z$, which follow the morphology characteristic of reported MXenes.[54] STEM analysis of single-flake $Ti_{2.7}Ta_{0.15}Hf_{0.15}C_2T_z$ shown in **Figure 3(b)** occurrence emphasizes the lateral distribution of the Ta and Hf substitutions, as these elements appear with brighter contrast compared to Ti in HAADF.

The chemical composition and surface elemental valence state of the Hf-substituted $Ti_{2.85}Hf_{0.15}C_2T_z$ and the Ta-Hf co-substituted $Ti_{2.7}Ta_{0.15}Hf_{0.15}C_2T_z$ MXenes were studied with XPS and shown in the **Figure 4**. While XPS of Ta-substituted $Ti_3C_2T_z$ has previously been reported,[37] the addition of Hf and Ta-Hf (co-substitution) is expected to further alter the electronic structure of the metals within the flake.

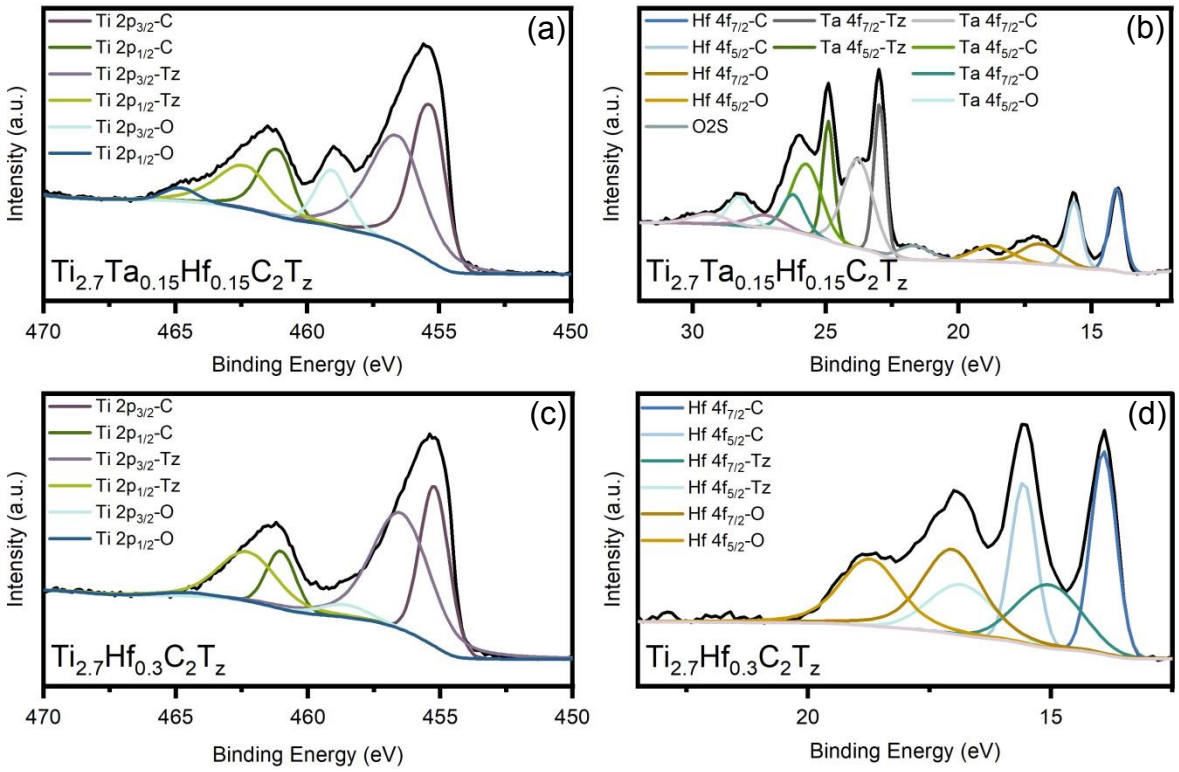

View Article Online
DOI: 10.1039/D6TA00700G

Figure 4. *XPS spectra for the $Ti_{2.7}Ta_{0.15}Hf_{0.15}C_2T_z$ and $Ti_{2.7}Hf_{0.3}C_2T_z$ core levels of (a) Ti 2p, (b) Ta 4f and Hf 4f, and the $Ti_{2.7}Hf_{0.3}C_2T_z$ core levels of (c) Ti 2p and (d) Hf 4f show different chemical environments.*

Figure 4(a) shows the Ti 2p core electron spectrum of in the Ta-Hf co-substituted $Ti_{2.7}Ta_{0.15}Hf_{0.15}C_2T_z$ with peaks characteristic for $Ti_3C_2T_z$-type MXenes. The peaks at binding energies (BEs) of 455.4 eV (Ti $2p_{3/2}$) and 461.2 eV (Ti $2p_{1/2}$) are attributed to Ti-C bonding. Moreover, the peaks at BE values of 456.7 eV and 462.5 eV, which correspond to the spin orbit coupling pair of Ti $2p_{3/2}$ and Ti $2p_{1/2}$, occurred due to the Ti-C_z bond (where z represents the -O, -F, and OH functional groups present at the surface of the MXene).[55,56] Further, the partially oxidized surface of the Ta-Hf co-substituted $Ti_{2.7}Ta_{0.15}Hf_{0.15}C_2T_z$ was observed at BE values of 459.1 eV and 464.8 eV, which correspond to the Ti-O bond, and is regularly observed in as-synthesized $Ti_3C_2T_z$.[57,58] Ta 4f and Hf 4f XPS spectra were deconvolved and shown in **Figure 4(b)**. Peaks at 14.3 eV (Hf $4f_{7/2}$) and 15.9 eV (Hf $4f_{5/2}$) are attributed to Hf-C bonding, whereas the peaks at 23.80 eV (Ta $4f_{7/2}$) and 25.74 eV (Ta $4f_{5/2}$) in the same spectrum are from Ta-C bonding.

By comparison, XPS of Ti and Hf for the Hf-substituted (i.e., no Ta) $Ti_{2.7}Hf_{0.3}C_2T_z$ are shown in **Figure 4(c)** and **Figure 4(d)**, respectively. Importantly, the total Ti content remained the same in both samples. The metals in the as-synthesized Hf-substituted $Ti_{2.7}Hf_{0.3}C_2T_z$ MXene appear more oxidized compared to the co-substituted $Ti_{2.7}Ta_{0.15}Hf_{0.15}C_2T_z$ MXene, suggesting that the presence of Ta has a significant effect on the electronic structure. This effect was quantified by deconvoluting the XPS spectra and calculating how the relative fraction of M-C, M-O, and M-T_z bonding in as-synthesized MXenes varied between the unsubstituted ($Ti_3C_2T_z$), Ta-substituted ($Ti_{2.85}Ta_{0.3}C_2T_z$), Hf-substituted ($Ti_{2.7}Hf_{0.3}C_2T_z$), and Ta-Hf co-substituted ($Ti_{2.7}Ta_{0.15}Hf_{0.15}C_2T_z$) MXenes, as shown in **Table 2**.

View Article Online
DOI: 10.1039/D6TA00700G

Table 2. *Fraction of the bonds of each metal in $Ti_3C_2T_z$, $Ti_{2.7}Ta_{0.3}C_2T_z$, $Ti_{2.7}Hf_{0.3}C_2T_z$ and $Ti_{2.7}Ta_{0.15}Hf_{0.15}C_2T_z$. M stands for metal, either Ti, Ta or Hf:*

Element	Ti $2p_{3/2}$				Ta $4f_{7/2}$		Hf $4f_{7/2}$	
Sample / Bond	Unsubstituted at.%	Hf-substituted at.%	Ta substituted at.%	Ta-Hf co-substituted at.%	Ta-substituted at.%	Ta-Hf co-substituted at.%	Hf-substituted at.%	Ta-Hf co-substituted at.%
M-C	60.32	34.29	22.26	41.08	3.34	47.47	34.71	49.31
M-O	4.50	5.00	17.94	13.06	17.68	21.90	37.85	24.99
M-Tz	35.17	60.70	59.80	45.86	78.98	30.62	27.44	25.69

XPS data revealed that in the Ti $2p_{3/2}$ spectrum, the Ti-C contribution decreased from 60.32% to 34.29% as a result of Hf substitution, while Ti-T_z increased from 35.17% to 60.70%, indicating enhanced termination coverage with Hf substitution. For the Ta-substituted $Ti_{2.7}Ta_{0.3}C_2T_z$, the Ti $2p_{3/2}$ comprised of 22.26% Ti-C, 59.8% Ti-T_z, and 17.94% Ti-O, reflecting increased termination coverage accompanied by a notable rise in oxide content relative to the unsubstituted sample. For the Ta-Hf co-substituted material, the Ti $2p_{3/2}$ components shifted to 41.08% Ti-C, 45.86% Ti-T_z, and 13.06% Ti-O, suggesting partial recovery of carbide bonding and reduced oxide content compared to the Ta-only case. In the Hf $4f_{7/2}$ region, $Ti_{2.7}Hf_{0.3}C_2T_z$ showed 37.85% Hf-O, 34.71% Hf-C, and 27.44% Hf-T_z, while in the case of the Ta-Hf co-substituted sample, Hf-C increased to 49.31% and Hf-O decreased to 24.99%, evidencing suppressed Hf oxidation when co-substituted with Ta. In the Ta $4f_{7/2}$ region, the Ta-only sample exhibited 78.98% Ta-T_z, 17.68% Ta-O, and 3.34% Ta-C, indicating that Ta strongly participated in termination bonding rather than forming carbides. The larger presence of termination bonds as measured by XPS can also be evidence of the inclusion of defects within the MXene upon doping.

In contrast, the Ta-Hf co-substituted material contained 47.47% Ta-C, 30.62% Ta-T_z, and 21.90% Ta-O, marking the emergence of carbide and termination-bound Ta alongside a

View Article Online
DOI: 10.1039/D6TA00700G

modest decrease in Ta oxide compared to the Ta-only case. These changes support a cooperative effect in which oxyphilic Hf preferentially accommodates oxygen, while Ta stabilizes carbide and termination states, thereby suppressing bulk oxide growth and stabilizing the surface chemistry. This effect could be rationalized by the strong carbide stability of Ta and the high oxyphilicity of Hf, which drives Hf toward oxidation while Ta competes for oxygen and stabilized carbide/termination states, altering oxide nucleation energetics, and promoting mixed terminations that suppress HfO_2 formation. This trend, therefore, suggests a synergistic effect between Ta and Hf, in which Ta stabilized Hf in its carbide form and suppressed its surface oxidation. Given the uncertainties associated with peak fitting and the surface sensitivity of XPS, the extracted fractions should be treated as semi-quantitative. In addition, the electronic structure of the of the MXene mainly ruled by Ti 3d state near the fermi energy level, arising from strong hybridization between Ti 3d and C 2p orbitals.[59] This outcome high electrical conductivity but also localized electron density around Ti, which can act as a reactive center. Due to co-doping of Ta and Hf at the Ti site, substantial alteration of the electronic structure attributed to the introduction of more 5d orbitals. The hybridization between Ti 3d, Ta 5d, Hf 5d and C 2p states strengthen the M-C bond and widen the density of state near the fermi level. This electronic modification reduces the density of high energy reactive centers and enhances the lattice stability. Moreover, co-substitution of Ta and Hf gives better electronic compensation to single metal doping. As a result, Ta and Hf co-substituted MXene phase shows improved structural robustness and better resistance to oxidation than that of pristine MXene.[60]

Accordingly, we focus on relative trends rather than absolute compositions. The electrochemical corrosion study was carried out using forced anodic polarization curves.

Electrochemical Oxidation and Passivation Behavior

View Article Online
DOI: 10.1039/D6TA00700G

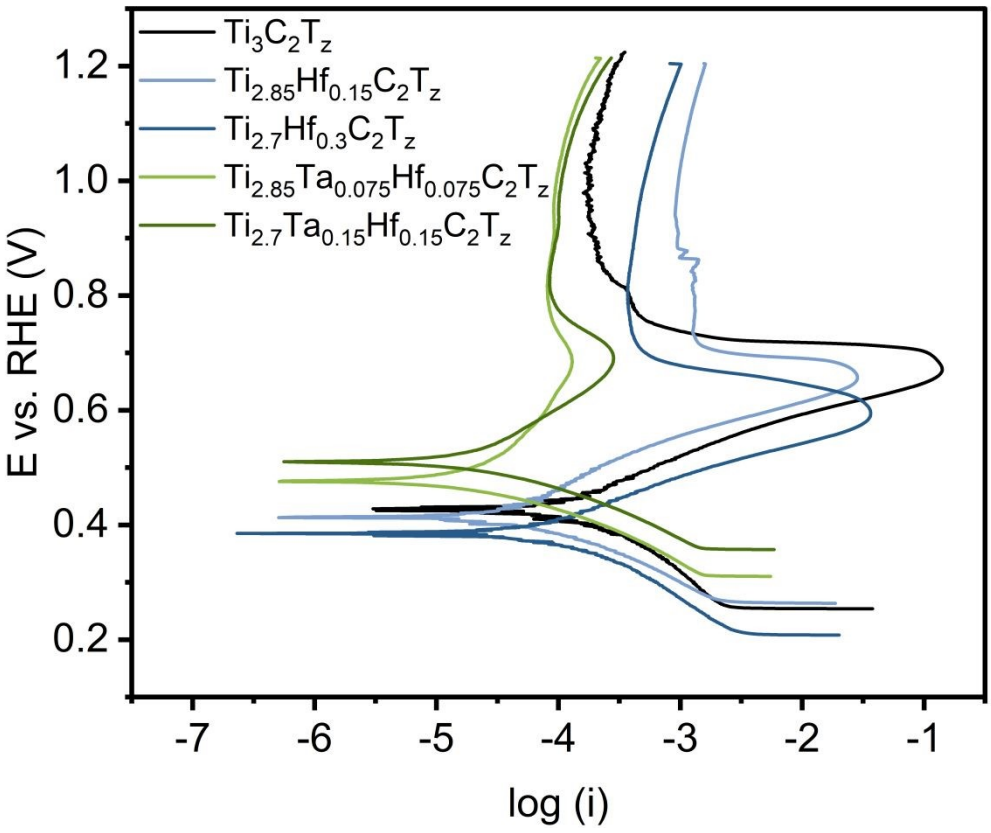

Figure 5. *Potentiodynamic anodic polarization curves for the native $Ti_3C_2T_z$, Hf-substituted $Ti_{2.85}Hf_{0.15}C_2T_z$, $Ti_{2.7}Hf_{0.3}C_2T_z$ and Ta-Hf co-substituted $Ti_{2.85}Ta_{0.075}Hf_{0.075}C_2T_z$, $Ti_{2.7}Ta_{0.15}Hf_{0.15}C_2T_z$ in N_2-saturated 0.5M H_2SO_4 at a potential scan rate of 0.167 mV/s.*

Figure 5 shows a comparison of potentiodynamic anodic corrosion curves of $Ti_3C_2T_z$, $Ti_{2.85}Hf_{0.15}C_2T_z$ $Ti_{2.7}Hf_{0.3}C_2T_z$, $Ti_{2.85}Ta_{0.075}Hf_{0.075}C_2T_z$, and $Ti_{2.7}Ta_{0.15}Hf_{0.15}C_2T_z$, at a potential scan rate of 0.167 mV/s in 0.5 M H_2SO_4 electrolyte solution.

Table 3. *Data derived from the potentiodyanamic anodic corrosion curves of as-synthesized materials.*

Sample Name	Ecorr [mV vs RHE]	I_{corr} [µA]	E_{pp} [mV vs RHE]	I_p[µA]
$Ti_3C_2T_z$	428	0.098	671.1	14.00
$Ti_{2.85}Ta_{0.075}Hf_{0.075}C_2T_z$	486	0.036	695.1	0.132
$Ti_{2.7}Ta_{0.15}Hf_{0.15}C_2T_z$	522	0.033	701.6	0.291
$Ti_{2.85}Hf_{0.15}C_2T_z$	423	0.025	656.8	28.44
$Ti_{2.7}Hf_{0.3}C_2T_z$	398	0.041	593.4	36.48

View Article Online
DOI: 10.1039/D6TA00700G

The reproducibility of measurements was ensured by repeating the experiments three times. The co-substitution of Ta and Hf exhibited substantial improvement in the corrosion potential (E_{corr}) compared to the pristine $Ti_3C_2T_z$, with an increase of 58 mV and 94 mV for $Ti_{2.85}Ta_{0.075}Hf_{0.075}C_2T_z$ and $Ti_{2.7}Ta_{0.15}Hf_{0.15}C_2T_z$ respectively. The noticeable enhancement widens the electrochemical stability range of the MXene based catalysts and improves their suitability and selectivity for the electrochemical applications. Additionally, there is a substantial decrease in the average kinetic current in the case of 5% and 10% Ta-Hf co-substituted MXene compared to the pristine MXene. Furthermore, the passivation potentials of the $Ti_{2.85}Ta_{0.075}Hf_{0.075}C_2T_z$ and $Ti_{2.7}Ta_{0.15}Hf_{0.15}C_2T_z$ were improved by 24 mV and 31 mV, respectively. The enhancement in the passivation potential may be due to the synergistically formation of Ta_2O_5 and HfO_2. Additionally, during the electrochemical corrosion test, the Ta and Hf have the ability to form stable oxides such as Ta_2O_5 and HfO_2, which synergistically prevent the oxidation of the Ti based MXene. In contrast, the Hf-substituted MXene showed a lower value of E_{corr} and E_{pp} compared to the pristine MXene.

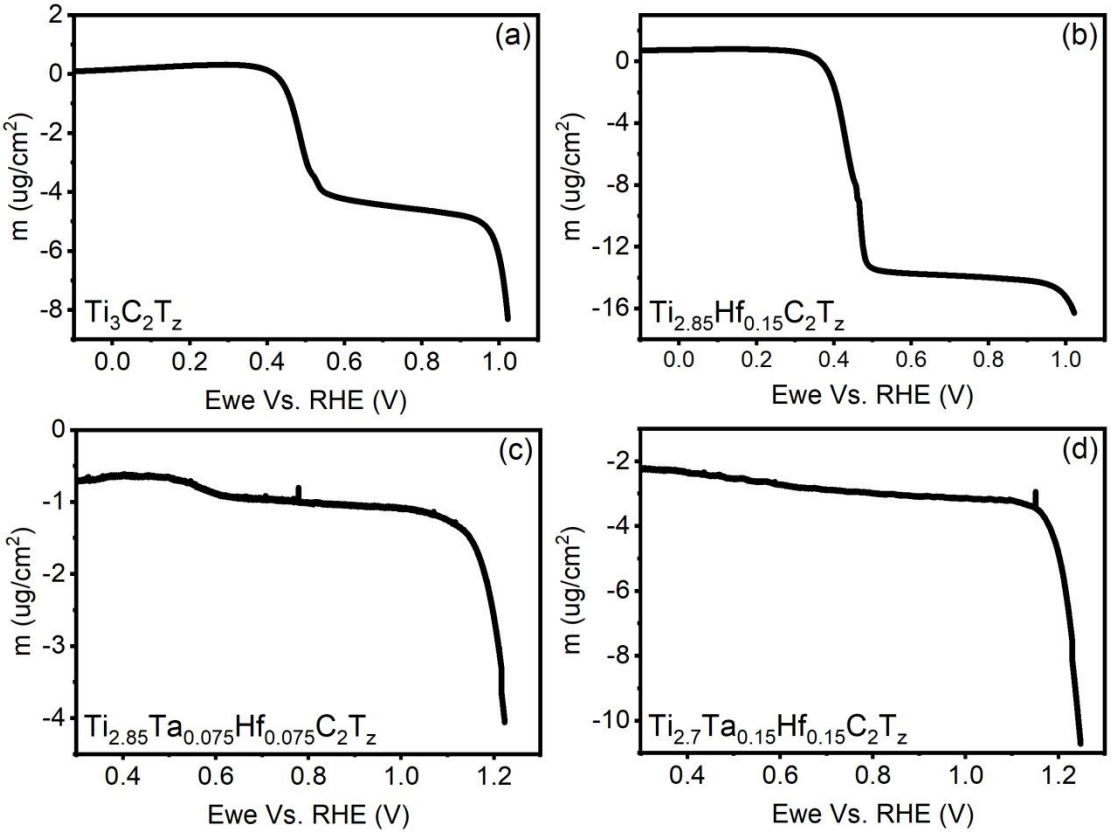

View Article Online
DOI: 10.1039/D6TA00700G

Figure 6. *(a) The comparative polarization curves of the $Ti_3C_2T_z$, $Ti_{2.85}Ta_{0.075}Hf_{0.075}C_2T_z$ and $Ti_{2.7}Ta_{0.15}Hf_{0.15}C_2T_z$ in N_2-saturated 0.5M H_2SO_4 at a potential scan rate of 0.167 mV/s. (b-d) Change in mass versus potential for $Ti_3C_2T_z$, $Ti_{2.85}Ta_{0.075}Hf_{0.075}C_2T_z$ and $Ti_{2.7}Ta_{0.15}Hf_{0.15}C_2T_z$ single layer flakes drop casted on TiAu EQCM electrode.*

An electrochemical quartz crystal microbalance (EQCM) was used to investigate change in mass of the electrode during the same forced electrochemical oxidation of the $Ti_3C_2T_z$, $Ti_{2.85}Hf_{0.15}C_2T_z$, $Ti_{2.85}Ta_{0.075}Hf_{0.075}C_2T_z$, and $Ti_{2.7}Ta_{0.15}Hf_{0.15}C_2T_z$ as described above, the results of which are shown in **Figure 6**.

EQCM measures apparent mass changes at the electrode surface during electrochemical cycling. Such mass variations can be consistent with processes such as oxidation, dissolution, passivation, or ion adsorption. However, EQCM alone cannot distinguish between these mechanisms or identify the chemical nature of the surface species.[61] Therefore, the observed mass changes are interpreted cautiously and discussed in conjunction with the electrochemical data. The pristine $Ti_3C_2T_z$ and $Ti_{2.85}Hf_{0.15}C_2T_z$ revealed significant mass loss during the primary oxidation step due to the degradation of the surface functional groups (-O, -OH and -F), leading to the reduction in mass as shown in **Figure 6(a)**. In the case of the Hf-substituted MXene formation of amorphous HfO_2, which may have dissolved in the electrolyte with increase in potential as depicted in **Figure 6(b)**. Moreover, once reaching the primary passivation potential (E_{pp}), the mass stabilizes due to of the formation of a protective oxide layer.

Interestingly, there was no significant mass loss during the primary oxidation step in the case of the Ta-Hf co-substituted $Ti_{2.85}Ta_{0.075}Hf_{0.075}C_2T_z$ and $Ti_{2.7}Ta_{0.15}Hf_{0.015}C_2T_z$ as shown in **Figure 6(c-d)**. This is consistent with the potentiodynamic anodic polarization curves in **Figure 5**, which showed significantly less oxidation current before reaching a passivation plateau. While the Hf-substituted MXene showed passivation behavior, the onset of oxidation was at significantly lower potentials, and the passivation currents were significantly higher compared to the Ta-Hf co-substituted MXene. This suggests that while Hf-substitution could slightly lower the passivation current compared to pristine MXene, only the co-substitution of Ta-Hf yielded improved performance with respect to arresting the oxidation process with increased electrochemical potential. DFT calculations have

View Article Online
DOI: 10.1039/D6TA00700G

shown [56,62] that the dissociation enthalpy for Ta-O is slightly larger than that of Hf-O, and yet, the oxyphilicity of Ta was slightly lower than that of Hf , although quantitative comparison of oxyphilicity is limited by the lack of normalization data for Hf. Therefore, the stability resulting from the addition of Ta may be related to the stability of the formed oxides (i.e., Ta_2O_5 and HfO_2), and less likely due to the inherent oxyphilicity of Ta by comparison to Hf.

View Article Online
DOI: 10.1039/D6TA00700G

Element-Resolved Corrosion and Structural Integrity

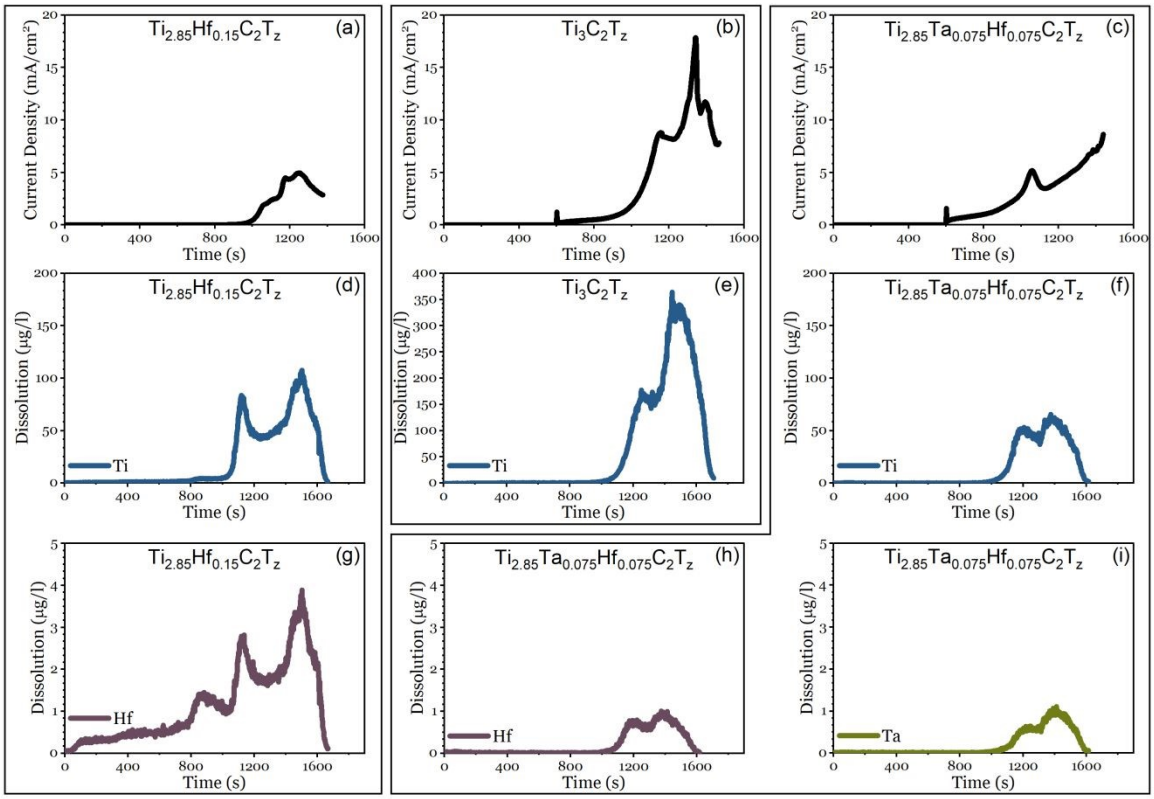

Figure 7. *In-situ ICP-MS flow cell measurements of $Ti_3C_2T_z$ (a-d), $Ti_{2.85}Hf_{0.15}C_2T_z$ (b,e,g), and $Ti_{2.85}Hf_{0.075}Ta_{0.075}C_2T_z$ (c,f,h–i). (a–c) Current density, (d–f) Ti dissolution, (g,h) Hf dissolution, and (i) Ta dissolution. OCP (0.35 V vs. RHE) was held for 600s and then ramped to 1.2V vs RHE at a rate of 1 mV/s.*

In-situ ICP-MS was used to track the water-soluble corrosion products of pristine, Hf-substituted and Ta-Hf co-substituted $Ti_3C_2T_z$ during forced anodic polarization similar to the procedure used in **Figure 5**. As seen from **Figure 7.d** ICP-MS of pristine $Ti_3C_2T_z$ showed significant Ti dissolution starting at 1025s (0.7 V), in alignment with the increased current. The amount of Ti lost to anodic corrosion dropped significantly with Hf substitution (Figure 7.e), and even more significantly with Ta-Hf co-substitution (Figure 7.f) (at the same overall substitution level for Ti at the MXene with only Hf-substitution). Additionally, as seen in Figure 7.h, the amount of Hf measured by the ICP-MS noticeably dropped with the simultaneous addition of Ta. Importantly, the ICP-MS does not fully characterize the corrosion processes of the MXene flakes, but rather, only corrosion processes which lead to soluble corrosion products which are flushed away from the cell

View Article Online
DOI: 10.1039/D6TA00700G

and fed into the ICP-MS. Metal leaching from electrodes during electrochemical operation is a significant barrier to electrode durability since its occurrence is typically irreversible. The ICP-MS result (as shown in **Figure 7. f,h-i**) of the Ta-Hf co-substituted MXene therefore suggests that the co-doping strategy plays an important role in mitigating the overall corrosion (as described by the current density) and the formation of soluble corrosion products leading to irreversible damage, as shown by the metal content in the ICP-MS during anodic polarization. We believe that the mechanism by which the dissolution of Ti is reduced by the addition of Ta and Hf (and likewise the dissolution of Hf by the addition of Ta) has to do with favoring the forming non-soluble corrosion products based on Ta_2O_5 and HfO_2. This hypothesis comes from XPS, which indicates that the termination coverage and surface carbide composition (and hence corrosion product composition) varied dramatically upon Hf, Ta, and Hf-Ta co-substitution.

In order to corroborate chemical information, the structural effects of corrosion during potentiodyanamic anodic polarization was analyzed here using TEM and reported by the authors previously.[37] Given the fact that the Ta-Hf co-substituted MXene showed the best performance in the forced anodic polarization tests, $Ti_{2.7}Ta_{0.15}Hf_{0.15}C_2T_x$ was analyzed using TEM and shown in **Figure 8**.

Figure 8(a) shows the flakes of $Ti_{2.7}Ta_{0.15}Hf_{0.15}C_2T_z$ before electrochemical oxidation treatment whereas **Figure 8(b) and Figure S6** shows the TEM and HR-TEM images of flakes after electrochemical corrosion testing conducted up to 0.9 V vs. RHE at a potential sweep rate of 0.167 mV/s in an acidic electrolyte (0.5 M H_2SO_4).

View Article Online
DOI: 10.1039/D6TA00700G

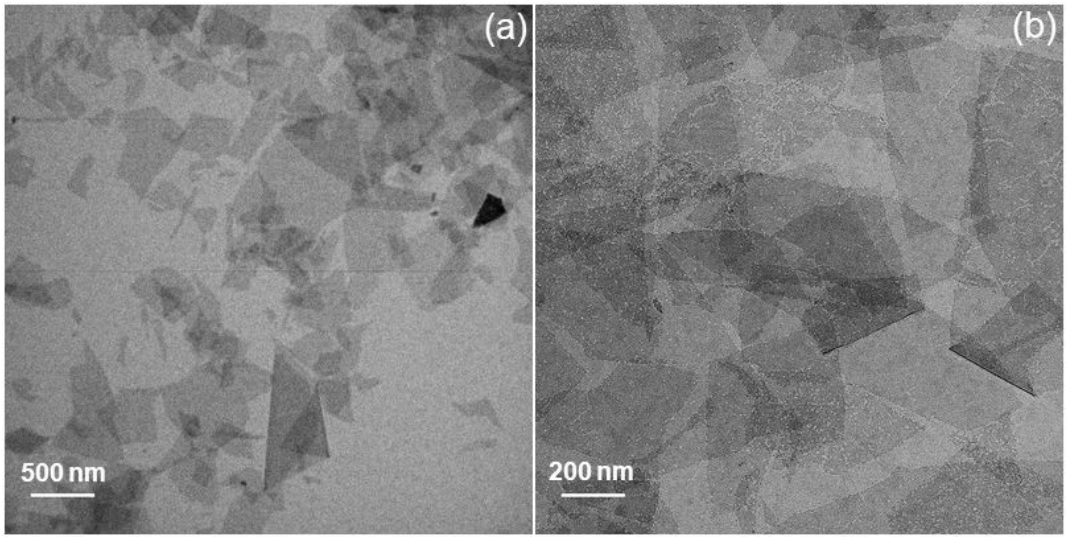

Figure 8 *(a) Bright-field TEM image of the pristine $Ti_{2.7}Ta_{0.15}Hf_{0.15}C_2T_z$. (b) Bright-field TEM images of the $Ti_{2.7}Ta_{0.15}Hf_{0.15}C_2T_z$ after scanning to the 0.9 V vs. RHE at 0.167 mV/s scan rate in the 0.5M H_2SO_4.*

TEM shows that $Ti_{2.7}Ta_{0.15}Hf_{0.15}C_2T_z$ retained its original shape with edges remaining sharp and straight after electrochemical oxidation treatment. This contrasts with unsubstituted $Ti_3C_2T_z$ flakes reported by us[37] and others[34] whose edges and size undergo a dramatic change as a result of oxidation after the same (or similar) treatment. During oxidation of the Ta-Hf co-substituted MXene, 10-20 nm holes were observed on the basal plane of the flakes. The hole formation is likely associated with localized oxidation during anodic polarization, forming localized vacancies on its basal plane that served as initiation points for further oxidative attack rather than oxidation on its edges as seen in pristine MXene.[37] The occurrence of holes is due to the favored oxidation of Ta and Hf (compared to Ti), which altered how the flake oxidized and ultimately increased its durability under positive electrochemical potentials.

PEM Fuel Cell Measurement

Finally, 40 wt.% platinum was loaded on the as-synthesized MXenes, and designated here as $Pt/Ti_3C_2T_z$, $Pt/Ti_{2.85}Hf_{0.15}C_2T_z$, $Pt/Ti_{2.7}Hf_{0.3}C_2T_z$ $Pt/Ti_{2.85}Ta_{0.075}Hf_{0.075}C_2T_z$ and $Pt/Ti_{2.7}Ta_{0.15}Hf_{0.15}C_2T_z$. Pt loading on the MXene ($Pt/Ti_{2.7}Ta_{0.15}Hf_{0.15}C_2T_z$) flake was observed using TEM (**Figure S7**). The TEM image shows the uniform distribution of Pt particles on the MXene flake, with an average particle size of 4.2 nm. A single-cell 5 cm^2

View Article Online
DOI: 10.1039/D6TA00700G

PEMFC was used to evaluate the performance of the variously substituted Pt-loaded MXene catalysts employed at the anode. While the use of the MXene at the anode does not completely parallel the corrosion tests reported above, owing to the flow of hydrogen, anode reversal tests simulating extreme fuel starvation were performed to reach the highly positive potentials known to cause degradation in PEMFCs during startup-up and shut-down operations.[63]

Figure S8 shows the polarization curves of the Pt/$Ti_3C_2T_z$, Pt/$Ti_{2.85}Hf_{0.15}C_2T_z$, Pt/$Ti_{2.7}Hf_{0.3}C_2T_z$, Pt/$Ti_{2.85}Ta_{0.075}Hf_{0.075}C_2T_z$, and Pt/$Ti_{2.7}Ta_{0.15}Hf_{0.15}C_2T_z$. Among all the catalysts, Pt/$Ti_{2.7}Ta_{0.15}Hf_{0.15}C_2T_z$ showed substantially improved performance. This represents a significant accomplishment in catalyst support development, as the co-substituted MXene support shows both better performance and better durability, as shown in **Figure 5** and **Figure 6** and discussed further below. Typically, improvements in durability come at the expense of activity, and vice versa.[64,65]

The impact of Hf- and Ta-substitution on catalyst durability was tested using an AST, which included cycling the cell between 0.6 and 0.9 V for up to 20k electrochemical cycles. The polarization curves before and after 20k cycles of the Pt/$Ti_3C_2T_z$, Pt/$Ti_{2.7}Ta_{0.15}Hf_{0.15}C_2T_z$, Pt/$Ti_{2.85}Ta_{0.075}Hf_{0.075}C_2T_z$ and Pt/$Ti_{2.85}Ta_{0.15}C_2T_z$ when used as anode catalyst and commercially available Pt/C catalyst coated Nafion NR-212 membrane used as cathode in full cell are represented in **Figure 9, Figure S9(a)** and **Figure S10**, respectively. As a result, after 20k cycles, the Pt/$Ti_3C_2T_z$ supported anode was degraded by 39 mV, as shown in **Figure 9(a)**. Impressively, in the case of the Pt/$Ti_{2.7}Ta_{0.15}Hf_{0.15}C_2T_z$ (**Figure 9(b)**) anode degradation was only 9 mV at 0.6 A/cm^2 under the same electrochemical cycling test after 20k cycles. In addition, Pt/$Ti_{2.7}Ta_{0.15}Hf_{0.15}C_2T_z$ exhibited a degradation trend comparable to that of Pt/$Ti_{2.85}Ta_{0.15}C_2T_z$ (**Figure S10**), tested in our previous work. [37]

The anode reversal degradation test was performed to investigate the sustainability of the anode under severe fuel starvation. In this test, the anode side of the fuel cell was purged with humidified nitrogen (N_2) and a constant current density of 0.2 A/cm^2 was applied, causing a sudden drop in cell voltage (i.e., a dramatic increase in anode voltage). Furthermore, the system changes were monitored for 2 hours under the applied reversal

View Article Online
DOI: 10.1039/D6TA00700G

condition. After the anode reversal test, the cell was conditioned, and the polarization curve was measured to evaluate the performance after the anode reversal test.

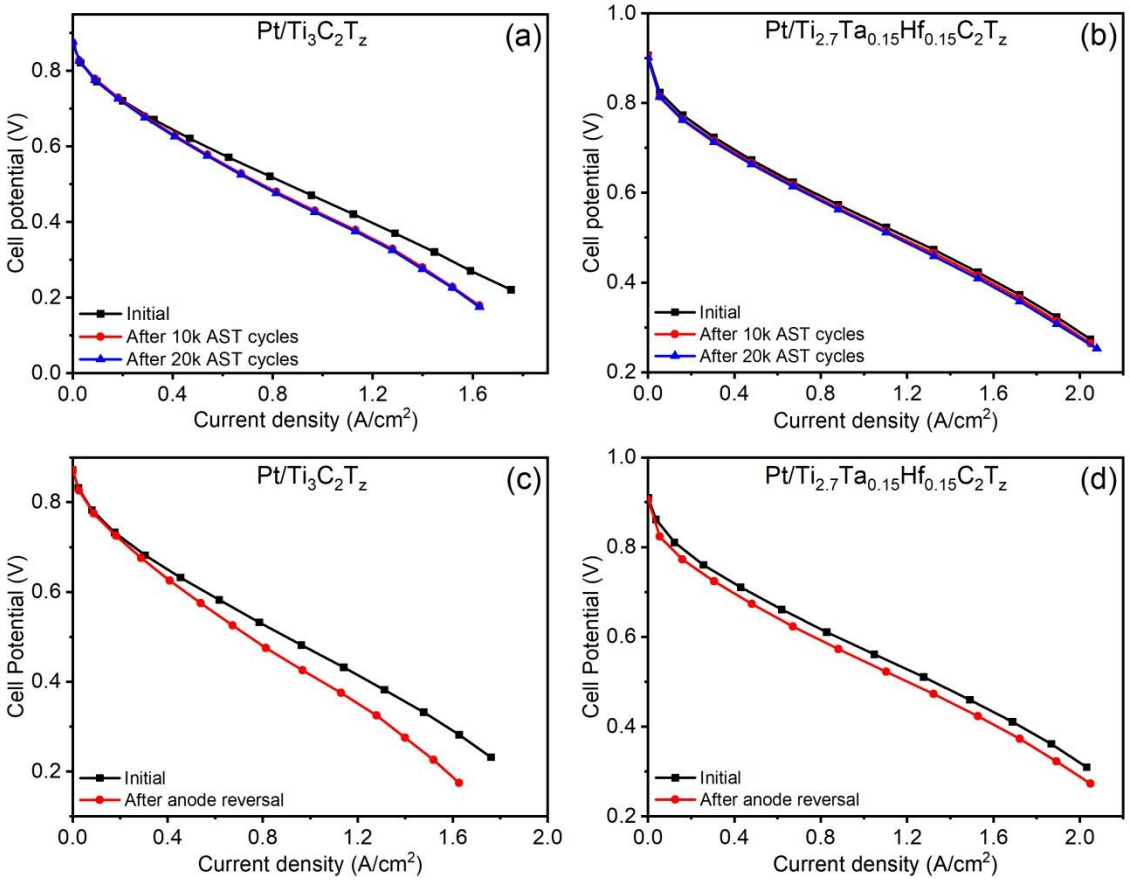

Figure 9. *Comparative AST polarization curves of fuel cell cycled between 0.6 to 0.9 V using state-of-the-art Pt/C cathode and Pt anode supported by (a) $Ti_3C_2T_z$ and (b) $Ti_{2.7}Ta_{0.15}Hf_{0.15}C_2T_z$. Polarization curves for 5 cm^2 fuel cell using Pt/C cathode and a Pt supported by (c) $Ti_3C_2T_z$ and (d) $Ti_{2.7}Ta_{0.15}Hf_{0.15}C_2T_z$ before and after anode reversal measurement.*

Figure 9(c-d) and **Figure S9(b)** show the polarization curves $Pt/Ti_3C_2T_z$, $Ti_{2.7}Ta_{0.15}Hf_{0.15}C_2T_z$ and $Pt/Ti_{2.85}Ta_{0.075}Hf_{0.075}C_2T_z$ as anode in fuel cell before and after the anode reversal test, respectively. The results of the anode reversal sustainability study are consistent with those obtained from the AST test, indicating that Pt-loaded $Ti_{2.7}Ta_{0.15}Hf_{0.15}C_2T_z$ anode shows superior performance compared to $Ti_3C_2T_z$ supported Pt anode in a fuel cell. Moreover, TEM analysis was carried out to examine the surface changes of the electrocatalyst $Pt/Ti_{2.7}Ta_{0.15}Hf_{0.15}C_2T_z$ after 20k AST. **Figure S11** reveals the TEM images of the $Pt/Ti_{2.7}Ta_{0.15}Hf_{0.15}C_2T_x$ after the AST test. **Figure S11** reveals no

View Article Online
DOI: 10.1039/D6TA00700G

significant change in the morphology of the Pt/$Ti_{2.7}Ta_{0.15}Hf_{0.15}C_2T_z$, whereas Pt particles start to agglomerate, which confirms the stable nature of the catalyst.

Overall, all the results suggest that 10 at. % co-substituted Ta and Hf MXene ($Ti_{2.7}Ta_{0.15}Hf_{0.15}C_2T_z$) shows significant enhancement in the electrochemical oxidation properties, which helps to improve the durability and sustainability of the support material in fuel cell technology.

Conclusions

$Ti_3C_2T_z$ MXenes were modified through hafnium substitution and tantalum–hafnium co-substitution to investigate how oxyphilic metal incorporation influences anodic electrochemical stability and durability. While single Hf substitution provided limited improvement, Ta–Hf co-substitution significantly suppressed anodic corrosion, reduced metal dissolution, and extended the electrochemical stability window to more positive potentials. Operando dissolution measurements and surface analysis reveal that co-substitution stabilizes the MXene surface chemistry by suppressing titanium oxide formation and promoting the formation of protective mixed oxides. When employed as catalyst supports in proton exchange membrane fuel cells, Pt-loaded Ta–Hf co-substituted MXenes exhibited markedly improved durability under accelerated stress testing and anode reversal conditions compared to pristine and singly substituted MXenes. These findings demonstrate that oxyphilic metal co-substitution is an effective and general materials design strategy to stabilize MXenes under anodic conditions, enabling their use as durable catalyst supports in fuel cell and other electrochemical energy conversion applications.

Authors Contribution

Haridas Parse and Danielle Sviri Belilty: conceptualization, experiments, data curation, validation, investigation, writing-original draft, review and editing. Bar Favelukis: investigation, review and editing. Mathias Krämer: ICP-MS experiment and analysis. Andrea M. Mingers: review and editing. Sukanta Chakrabartty: investigation. Noam Eliaz: review and editing. Baptiste Gault: review and editing. Dierk Raabe: review and editing. Maxim Sokol and Brian Rosen: funding, supervision, writing-review and editing.

Acknowledgments

View Article Online
DOI: 10.1039/D6TA00700G

The authors wish to acknowledge funding by the Deutsche Forschungsgemeinschaft (DFG) grant (EL 869/1-1 RA 659/30-1) through the German Research Foundation (DFG). The authors acknowledge Dr. George Levi, Dr. Pini Shekhter, and Alexander Gordin from the Center for Nanoscience and Nanotechnology, Tel Aviv University, for TEM, STEM-EDS, ICP-MS, and XPS characterization. The authors also acknowledge Dr. Nitzan Maman, Dr. Alexander Upcher, and Dr. Vladimir Ezersky from the Ilse Katz Institute for Nanoscale Science and Technology, Ben-Gurion University of the Negev, for FIB preparation and HR-TEM measurements.

Conflict of Interest

The authors declare no conflict of interest.

References

(1) Hamo, E. R.; Rosen, B. A. Transition Metal Carbides as Cathode Supports for PEM Fuel Cells. *Nano Research*. Tsinghua University December 1, 2022, pp 10218–10233. https://doi.org/10.1007/s12274-022-4831-3.

(2) Boni, M.; Manikanta, C. S.; Velisala, V. Experimental Evaluation of Proton Exchange Membrane Fuel Cell Performance with Sinusoidal Flow Channel Designs. *Int. J. Hydrogen Energy* **2024**, *53*, 1233–1241. https://doi.org/10.1016/j.ijhydene.2023.11.340.

(3) Meier, J. C.; Galeano, C.; Katsounaros, I.; Witte, J.; Bongard, H. J.; Topalov, A. A.; Baldizzone, C.; Mezzavilla, S.; Schüth, F.; Mayrhofer, K. J. J. Design Criteria for Stable Pt/C Fuel Cell Catalysts. *Beilstein Journal of Nanotechnology*. 2014, pp 44–67. https://doi.org/10.3762/bjnano.5.5.

(4) Celorrio, V.; Flórez-Montaño, J.; Moliner, R.; Pastor, E.; Lázaro, M. J. Fuel Cell Performance of Pt Electrocatalysts Supported on Carbon Nanocoils. In *International Journal of Hydrogen Energy*; 2014; Vol. 39, pp 5371–5377. https://doi.org/10.1016/j.ijhydene.2013.12.198.

(5) Tackett, B. M.; Sheng, W.; Chen, J. G. Opportunities and Challenges in Utilizing Metal-Modified Transition Metal Carbides as Low-Cost Electrocatalysts. *Joule*. Cell Press October 11, 2017, pp 253–263. https://doi.org/10.1016/j.joule.2017.07.002.

(6) Binninger, T.; Fabbri, E.; Kötz, R.; Schmidt, T. J. Determination of the Electrochemically Active Surface Area of Metal-Oxide Supported Platinum Catalyst. *J. Electrochem. Soc.* **2014**, *161* (3), H121–H128. https://doi.org/10.1149/2.055403jes.

(7) Ortiz-Herrera, J. C.; Cruz-Martínez, H.; Solorza-Feria, O.; Medina, D. I. Recent Progress in Carbon Nanotubes Support Materials for Pt-Based Cathode Catalysts in PEM Fuel Cells. *Int. J. Hydrogen Energy* **2022**, *47* (70), 30213–30224. https://doi.org/10.1016/j.ijhydene.2022.03.218.

View Article Online
DOI: 10.1039/D6TA00700G

(8) Schulenburg, H.; Schwanitz, B.; Linse, N.; Scherer, G. G.; Wokaun, A.; Krbanjevic, J.; Grothausmann, R.; Manke, I. 3D Imaging of Catalyst Support Corrosion in Polymer Electrolyte Fuel Cells. *Journal of Physical Chemistry C* **2011**, *115* (29), 14236–14243. https://doi.org/10.1021/jp203016u.

(9) Mayrhofer, K. J. J.; Ashton, S. J.; Meier, J. C.; Wiberg, G. K. H.; Hanzlik, M.; Arenz, M. Non-Destructive Transmission Electron Microscopy Study of Catalyst Degradation under Electrochemical Treatment. *J. Power Sources* **2008**, *185* (2), 734–739. https://doi.org/10.1016/j.jpowsour.2008.08.003.

(10) Yoshimoto, N.; Niida, Y.; Egashira, M.; -, al; Han, K.-S.; Na -, J.-W. *Instability of Pt/C Electrocatalysts in Proton Exchange Membrane Fuel Cells: A Mechanistic Investigation You May Also like Used Lithium Ion Rechargeable Battery Recycling Using Etoile-Rebatt Technology Kyoo-Seung Han and Dongil Na-Nonflammable Gel Electrolyte Containing Alkyl Phosphate for Rechargeable Lithium Batteries Preparation of LiMn2O4 at the Low Temperature of 250 Degrees Using a Novel Eutectic Self-Mixing Method This Content Was Downloaded from IP Address*.

(11) Randrianarizafy, B.; Schott, P.; Gerard, M.; Bultel, Y. Modelling Carbon Corrosion during a PEMFC Startup: Simulation of Mitigation Strategies. *Energies (Basel)*. **2020**, *13* (9). https://doi.org/10.3390/en13092338.

(12) Shen, Q.; Hou, M.; Liang, D.; Zhou, Z.; Li, X.; Shao, Z.; Yi, B. Study on the Processes of Start-up and Shutdown in Proton Exchange Membrane Fuel Cells. *J. Power Sources* **2009**, *189* (2), 1114–1119. https://doi.org/10.1016/j.jpowsour.2008.12.075.

(13) Zhao, L.; Zhu, J.; Zheng, Y.; Xiao, M.; Gao, R.; Zhang, Z.; Wen, G.; Dou, H.; Deng, Y. P.; Yu, A.; Wang, Z.; Chen, Z. Materials Engineering toward Durable Electrocatalysts for Proton Exchange Membrane Fuel Cells. *Advanced Energy Materials*. John Wiley and Sons Inc January 1, 2022. https://doi.org/10.1002/aenm.202102665.

(14) Liu, Y.; Kelly, T. G.; Chen, J. G.; Mustain, W. E. Metal Carbides as Alternative Electrocatalyst Supports. *ACS Catalysis*. American Chemical Society June 7, 2013, pp 1184–1194. https://doi.org/10.1021/cs4001249.

(15) Kong, W.; Deng, J.; Li, L. Recent Advances in Noble Metal MXene-Based Catalysts for Electrocatalysis. *Journal of Materials Chemistry A*. Royal Society of Chemistry April 21, 2022, pp 14674–14691. https://doi.org/10.1039/d2ta00613h.

(16) Liu, A.; Liang, X.; Ren, X.; Guan, W.; Gao, M.; Yang, Y.; Yang, Q.; Gao, L.; Li, Y.; Ma, T. Recent Progress in MXene-Based Materials: Potential High-Performance Electrocatalysts. *Advanced Functional Materials*. Wiley-VCH Verlag September 1, 2020. https://doi.org/10.1002/adfm.202003437.

(17) Naguib, M.; Kurtoglu, M.; Presser, V.; Lu, J.; Niu, J.; Heon, M.; Hultman, L.; Gogotsi, Y.; Barsoum, M. W. Two-Dimensional Nanocrystals Produced by Exfoliation of Ti 3AlC 2. *Advanced Materials* **2011**, *23* (37), 4248–4253. https://doi.org/10.1002/adma.201102306.

(18) Shi, C.; Beidaghi, M.; Naguib, M.; Mashtalir, O.; Gogotsi, Y.; Billinge, S. J. L. Structure of Nanocrystalline Ti3 C2 MXene Using Atomic Pair Distribution Function. *Phys. Rev. Lett.* **2013**, *112* (12). https://doi.org/10.1103/PhysRevLett.112.125501.

View Article Online
DOI: 10.1039/D6TA00700G

(19) Mohammadi, A. V.; Rosen, J.; Gogotsi, Y. The World of Two-Dimensional Carbides and Nitrides (MXenes). *Science*. American Association for the Advancement of Science June 11, 2021. https://doi.org/10.1126/science.abf1581.

(20) Hong, S.; El-Demellawi, J. K.; Lei, Y.; Liu, Z.; Marzooqi, F. Al; Arafat, H. A.; Alshareef, H. N. Porous Ti3C2TxMXene Membranes for Highly Efficient Salinity Gradient Energy Harvesting. *ACS Nano* **2022**, *16* (1), 792–800. https://doi.org/10.1021/acsnano.1c08347.

(21) Halim, J.; Kota, S.; Lukatskaya, M. R.; Naguib, M.; Zhao, M. Q.; Moon, E. J.; Pitock, J.; Nanda, J.; May, S. J.; Gogotsi, Y.; Barsoum, M. W. Synthesis and Characterization of 2D Molybdenum Carbide (MXene). *Adv. Funct. Mater.* **2016**, *26* (18), 3118–3127. https://doi.org/10.1002/adfm.201505328.

(22) He, L.; Zhuang, H.; Fan, Q.; Yu, P.; Wang, S.; Pang, Y.; Chen, K.; Liang, K. Advances and Challenges in MXene-Based Electrocatalysts: Unlocking the Potential for Sustainable Energy Conversion. *Materials Horizons*. Royal Society of Chemistry August 22, 2024. https://doi.org/10.1039/d4mh00845f.

(23) Naguib, M.; Mochalin, V. N.; Barsoum, M. W.; Gogotsi, Y. 25th Anniversary Article: MXenes: A New Family of Two-Dimensional Materials. *Advanced Materials* **2014**, *26* (7), 992–1005. https://doi.org/10.1002/adma.201304138.

(24) Iqbal, A.; Hong, J.; Ko, T. Y.; Koo, C. M. Improving Oxidation Stability of 2D MXenes: Synthesis, Storage Media, and Conditions. *Nano Convergence*. Korea Nano Technology Research Society December 1, 2021. https://doi.org/10.1186/s40580-021-00259-6.

(25) Lipatov, A.; Goad, A.; Loes, M. J.; Vorobeva, N. S.; Abourahma, J.; Gogotsi, Y.; Sinitskii, A. High Electrical Conductivity and Breakdown Current Density of Individual Monolayer Ti3C2Tx MXene Flakes. *Matter* **2021**, *4* (4), 1413–1427. https://doi.org/10.1016/j.matt.2021.01.021.

(26) Guan, Y.; Zhang, M.; Qin, J.; Ma, X.; Li, C.; Tang, J. Hydrophilicity-Dependent Distinct Frictional Behaviors of Different Modified MXene Nanosheets. *Journal of Physical Chemistry C* **2020**, *124* (25), 13664–13671. https://doi.org/10.1021/acs.jpcc.0c01551.

(27) Bilibana, M. P. Electrochemical Properties of MXenes and Applications. *Advanced Sensor and Energy Materials* **2023**, *2* (4), 100080. https://doi.org/10.1016/j.asems.2023.100080.

(28) Zhang, Z.; Liu, C.; Dai, Y.; Liu, B.; Guo, P.; Tu, F.; Ma, M.; Shen, L.; Zhao, Z.; Liu, Y.; Zhang, Y.; Zhao, L.; Wang, Z. Sandwich-Structured MXene/Carbon Hybrid Support Decorated with Pt Nanoparticles for Oxygen Reduction Reaction. *ACS Appl. Energy Mater.* **2022**, *5* (12), 14957–14965. https://doi.org/10.1021/acsaem.2c02479.

(29) He, S.; Zhu, Q.; Soomro, R. A.; Xu, B. MXene Derivatives for Energy Storage Applications. *Sustainable Energy and Fuels*. Royal Society of Chemistry October 1, 2020, pp 4988–5004. https://doi.org/10.1039/d0se00927j.

(30) Lipatov, A.; Alhabeb, M.; Lukatskaya, M. R.; Boson, A.; Gogotsi, Y.; Sinitskii, A. Effect of Synthesis on Quality, Electronic Properties and Environmental Stability of Individual Monolayer Ti3C2 MXene Flakes. *Adv. Electron. Mater.* **2016**, *2* (12). https://doi.org/10.1002/aelm.201600255.

View Article Online
DOI: 10.1039/D6TA00700G

(31) Thakur, R.; Vahidmohammadi, A.; Moncada, J.; Adams, W. R.; Chi, M.; Tatarchuk, B.; Beidaghi, M.; Carrero, C. A. Insights into the Thermal and Chemical Stability of Multilayered V2CT: X MXene. *Nanoscale* **2019**, *11* (22), 10716–10726. https://doi.org/10.1039/c9nr03020d.

(32) Krämer, M.; Favelukis, B.; El-Zoka, A. A.; Sokol, M.; Rosen, B. A.; Eliaz, N.; Kim, S. H.; Gault, B. Near-Atomic-Scale Perspective on the Oxidation of Ti3C2Tx MXenes: Insights from Atom Probe Tomography. *Advanced Materials* **2024**, *36* (3). https://doi.org/10.1002/adma.202305183.

(33) Nayak, P.; Yang, M.; Wang, Z.; Li, X.; Miao, R.; Compton, R. G. Single-Entity Ti3C2Tx MXene Electro-Oxidation. *Appl. Mater. Today* **2022**, *26*. https://doi.org/10.1016/j.apmt.2021.101335.

(34) Tang, J.; Mathis, T. S.; Kurra, N.; Sarycheva, A.; Xiao, X.; Hedhili, M. N.; Jiang, Q.; Alshareef, H. N.; Xu, B.; Pan, F.; Gogotsi, Y. Tuning the Electrochemical Performance of Titanium Carbide MXene by Controllable In Situ Anodic Oxidation. *Angewandte Chemie* **2019**, *131* (49), 18013–18019. https://doi.org/10.1002/ange.201911604.

(35) Nayak, P.; Yang, M.; Wang, Z.; Li, X.; Miao, R.; Compton, R. G. Single-Entity Ti3C2Tx MXene Electro-Oxidation. *Appl. Mater. Today* **2022**, *26*. https://doi.org/10.1016/j.apmt.2021.101335.

(36) Lorencova, L.; Bertok, T.; Dosekova, E.; Holazova, A.; Paprckova, D.; Vikartovska, A.; Sasinkova, V.; Filip, J.; Kasak, P.; Jerigova, M.; Velic, D.; Mahmoud, K. A.; Tkac, J. Electrochemical Performance of Ti3C2Tx MXene in Aqueous Media: Towards Ultrasensitive H2O2 Sensing. *Electrochim. Acta* **2017**, *235*, 471–479. https://doi.org/10.1016/j.electacta.2017.03.073.

(37) Favelukis, B.; Chakrabartty, S.; Kumar, V.; Kim, S. H.; El-Zoka, A.; Krämer, M.; Raabe, D.; Gault, B.; Eliaz, N.; Natan, A.; Sokol, M.; Rosen, B. A. Improved Durability of Ti3C2Tz at Potentials above the Reversible Hydrogen Electrode by Tantalum Substitution. *Adv. Funct. Mater.* **2024**, *34* (10). https://doi.org/10.1002/adfm.202309749.

(38) Hong, W.; Wyatt, B. C.; Nemani, S. K.; Anasori, B. Double Transition-Metal MXenes: Atomistic Design of Two-Dimensional Carbides and Nitrides. *MRS Bulletin*. Cambridge University Press October 1, 2020, pp 850–861. https://doi.org/10.1557/mrs.2020.251.

(39) Ratzker, B.; Favelukis, B.; Baranov, M.; Rathod, Y.; Greenberg, A.; Messer, O.; Goldstein, D. A.; Upcher, A.; Ezersky, V.; Maman, N.; Biran, I.; Natu, V.; Sokol, M. Synthesis of Ti1-XWx Solid Solution MAX Phases and Derived MXenes for Sodium-Ion Battery Anodes. *Adv. Funct. Mater.* **2024**. https://doi.org/10.1002/adfm.202406499.

(40) Han, M.; Maleski, K.; Shuck, C. E.; Yang, Y.; Glazar, J. T.; Foucher, A. C.; Hantanasirisakul, K.; Sarycheva, A.; Frey, N. C.; May, S. J.; Shenoy, V. B.; Stach, E. A.; Gogotsi, Y. Tailoring Electronic and Optical Properties of MXenes through Forming Solid Solutions. *J. Am. Chem. Soc.* **2020**, *142* (45), 19110–19118. https://doi.org/10.1021/jacs.0c07395.

(41) Meng, F. L.; Zhou, Y. C.; Wang, J. Y. Strengthening of Ti2AlC by Substituting Ti with V. *Scr. Mater.* **2005**, *53* (12), 1369–1372. https://doi.org/10.1016/j.scriptamat.2005.08.030.

View Article Online
DOI: 10.1039/D6TA00700G

(42) Zuo, C.; Zhong, C. Screen the Elastic and Thermodynamic Properties of MAX Solid Solution Using DFT Procedue: Case Study on (Ti1-XVx)2AlC. *Mater. Chem. Phys.* **2020**, *250*. https://doi.org/10.1016/j.matchemphys.2020.123059.

(43) Wang, L.; Han, M.; Shuck, C. E.; Wang, X.; Gogotsi, Y. Adjustable Electrochemical Properties of Solid-Solution MXenes. *Nano Energy* **2021**, *88*. https://doi.org/10.1016/j.nanoen.2021.106308.

(44) Dahlqvist, M.; Rosen, J. Predictive Theoretical Screening of Phase Stability for Chemical Order and Disorder in Quaternary 312 and 413 MAX Phases. *Nanoscale* **2020**, *12* (2), 785–794. https://doi.org/10.1039/c9nr08675g.

(45) Rafieerad, A.; Yan, W.; Alagarsamy, K. N.; Srivastava, A.; Sareen, N.; Arora, R. C.; Dhingra, S. Fabrication of Smart Tantalum Carbide MXene Quantum Dots with Intrinsic Immunomodulatory Properties for Treatment of Allograft Vasculopathy. *Adv. Funct. Mater.* **2021**, *31* (46). https://doi.org/10.1002/adfm.202106786.

(46) Lim, K. R. G.; Shekhirev, M.; Wyatt, B. C.; Anasori, B.; Gogotsi, Y.; Seh, Z. W. Fundamentals of MXene Synthesis. *Nature Synthesis*. Nature Publishing Group August 1, 2022, pp 601–614. https://doi.org/10.1038/s44160-022-00104-6.

(47) Parse, H. B.; Patil, I.; Swami, A.; Kakade, B. An Adept Approach to Convert Titanium Carbide to Titanium Nitride and It's Composite with N-Doped Carbon Nanotubes for Efficient Oxygen Electroreduction Kinetics. *Catal. Today* **2021**, *370*, 46–54. https://doi.org/10.1016/j.cattod.2020.11.019.

(48) Alhabeb, M.; Maleski, K.; Anasori, B.; Lelyukh, P.; Clark, L.; Sin, S.; Gogotsi, Y. Guidelines for Synthesis and Processing of Two-Dimensional Titanium Carbide (Ti3C2Tx MXene). *Chemistry of Materials* **2017**, *29* (18), 7633–7644. https://doi.org/10.1021/acs.chemmater.7b02847.

(49) Shevchuk, K.; Sarycheva, A.; Shuck, C. E.; Gogotsi, Y. Raman Spectroscopy Characterization of 2D Carbide and Carbonitride MXenes. *Chemistry of Materials* **2023**, *35* (19), 8239–8247. https://doi.org/10.1021/acs.chemmater.3c01742.

(50) Handoko, A. D.; Fredrickson, K. D.; Anasori, B.; Convey, K. W.; Johnson, L. R.; Gogotsi, Y.; Vojvodic, A.; Seh, Z. W. Tuning the Basal Plane Functionalization of Two-Dimensional Metal Carbides (MXenes) to Control Hydrogen Evolution Activity. *ACS Appl. Energy Mater.* **2018**, *1* (1), 173–180. https://doi.org/10.1021/acsaem.7b00054.

(51) Natu, V.; Pai, R.; Wilson, O.; Gadasu, E.; Badr, H.; Karmakar, A.; Magenau, A. J. D.; Kalra, V.; Barsoum, M. W. Effect of Base/Nucleophile Treatment on Interlayer Ion Intercalation, Surface Terminations, and Osmotic Swelling of Ti3C2TzMXene Multilayers. *Chemistry of Materials* **2022**, *34* (2), 678–693. https://doi.org/10.1021/acs.chemmater.1c03390.

(52) Goossens, N.; Tunca, B.; Lapauw, T.; Lambrinou, K.; Vleugels, J. MAX Phases, Structure, Processing, and Properties. In *Encyclopedia of Materials: Technical Ceramics and Glasses: Volume 1-3*; Elsevier, 2021; Vol. 2, pp V2-182-V2-199. https://doi.org/10.1016/B978-0-12-818542-1.00015-1.

View Article Online
DOI: 10.1039/D6TA00700G

(53) Rigby, M. T. P.; Natu, V.; Sokol, M.; Kelly, D. J.; Hopkinson, D. G.; Zou, Y.; Bird, J. R. T.; Evitts, L. J.; Smith, M.; Race, C. P.; Frankel, P.; Haigh, S. J.; Barsoum, M. W. Synthesis of New M-Layer Solid-Solution 312 MAX Phases (Ta1-: XTix)3AlC2(x = 0.4, 0.62, 0.75, 0.91 or 0.95), and Their Corresponding MXenes. *RSC Adv.* **2021**, *11* (5), 3110–3114. https://doi.org/10.1039/d0ra09761f.

(54) Shekhirev, M.; Busa, J.; Shuck, C. E.; Torres, A.; Bagheri, S.; Sinitskii, A.; Gogotsi, Y. Ultralarge Flakes of Ti3C2TxMXene via Soft Delamination. *ACS Nano* **2022**, *16* (9), 13695–13703. https://doi.org/10.1021/acsnano.2c04506.

(55) Cao, Y.; Deng, Q.; Liu, Z.; Shen, D.; Wang, T.; Huang, Q.; Du, S.; Jiang, N.; Lin, C. Te; Yu, J. Enhanced Thermal Properties of Poly(Vinylidene Fluoride) Composites with Ultrathin Nanosheets of MXene. *RSC Adv.* **2017**, *7* (33), 20494–20501. https://doi.org/10.1039/C7RA00184C.

(56) Mashtalir, O.; Naguib, M.; Mochalin, V. N.; Dall'Agnese, Y.; Heon, M.; Barsoum, M. W.; Gogotsi, Y. Intercalation and Delamination of Layered Carbides and Carbonitrides. *Nat. Commun.* **2013**, *4*. https://doi.org/10.1038/ncomms2664.

(57) von Treifeldt, J. E.; Firestein, K. L.; Fernando, J. F. S.; Zhang, C.; Siriwardena, D. P.; Lewis, C. E. M.; Golberg, D. V. The Effect of Ti3AlC2 MAX Phase Synthetic History on the Structure and Electrochemical Properties of Resultant Ti3C2 MXenes. *Mater. Des.* **2021**, *199*. https://doi.org/10.1016/j.matdes.2020.109403.

(58) Tian, Z.; Tian, H.; Cao, K.; Bai, S.; Peng, Q.; Wang, Y.; Zhu, Q. Facile Preparation of Ti3C2Tx Sheets by Selectively Etching in a H2SO4/H2O2 Mixture. *Front. Chem.* **2022**, *10*. https://doi.org/10.3389/fchem.2022.962528.

(59) Khazaei, M.; Arai, M.; Sasaki, T.; Chung, C. Y.; Venkataramanan, N. S.; Estili, M.; Sakka, Y.; Kawazoe, Y. Novel Electronic and Magnetic Properties of Two-Dimensional Transition Metal Carbides and Nitrides. *Adv. Funct. Mater.* **2013**, *23* (17), 2185–2192. https://doi.org/10.1002/adfm.201202502.

(60) Kc, S.; Longo, R. C.; Addou, R.; Wallace, R. M.; Cho, K. Impact of Intrinsic Atomic Defects on the Electronic Structure of MoS 2 Monolayers. *Nanotechnology* **2014**, *25* (37). https://doi.org/10.1088/0957-4484/25/37/375703.

(61) Wittman, R. M.; Sacci, R. L.; Zawodzinski, T. A. Elucidating Mechanisms of Oxide Growth and Surface Passivation on Zinc Thin Film Electrodes in Alkaline Solutions Using the Electrochemical Quartz Crystal Microbalance. *J. Power Sources* **2019**, *438*. https://doi.org/10.1016/j.jpowsour.2019.227034.

(62) Kepp, K. P. A Quantitative Scale of Oxophilicity and Thiophilicity. *Inorg. Chem.* **2016**, *55* (18), 9461–9470. https://doi.org/10.1021/acs.inorgchem.6b01702.

(63) Soleymani, A. P.; Bonville, L.; Wang, C.; Schaefer, S.; Waldecker, J.; Jankovic, J. Quantifying Key Parameters to Provide Better Understating of Microstructural Changes in Polymer Electrolyte Membrane Fuel Cells during Degradation: A Startup/Shutdown Case Study. *J. Power Sources* **2023**, *563*. https://doi.org/10.1016/j.jpowsour.2023.232807.

(64) Saha, S.; Cabrera Rodas, J. A.; Tan, S.; Li, D. Performance Evaluation of Platinum-Molybdenum Carbide Nanocatalysts with Ultralow Platinum Loading on Anode and

View Article Online
DOI: 10.1039/D6TA00700G

Cathode Catalyst Layers of Proton Exchange Membrane Fuel Cells. *J. Power Sources* **2018**, *378*, 742–749. https://doi.org/10.1016/j.jpowsour.2017.12.062.

(65) Hamo, E. R.; Rosen, B. A. Improved Durability and Activity in Pt/Mo2C Fuel Cell Cathodes by Magnetron Sputtering of Tantalum. *ChemElectroChem* **2021**, *8* (16), 3123–3134. https://doi.org/10.1002/celc.202100591.

View Article Online
DOI: 10.1039/D6TA00700G

Data Availability Statement

The data supporting the findings of this study are available within the article and its Electronic Supplementary Information. Additional data are available from the corresponding author upon reasonable request.